GLOBAL ENERGETICS OF THIRTY-EIGHT LARGE SOLAR ERUPTIVE EVENTS

A. G. Emslie[1], B. R. Dennis[2], A. Y. Shih[2], P. C. Chamberlin[2], R. A. Mewaldt[3], C. S. Moore[4],
G. H. Share[5], A. Vourlidas[6], and B. T. Welsch[7]

[1] Department of Physics and Astronomy, Western Kentucky University, Bowling Green, KY 42101, USA; emslieg@wku.edu
[2] NASA Goddard Space Flight Center, Code 671, Greenbelt, MD 20771, USA; brian.r.dennis@nasa.gov, albert.y.shih@nasa.gov, phillip.c.chamberlin@nasa.gov
[3] Space Radiation Laboratory, California Institute of Technology, Pasadena, CA 91125, USA; rmewaldt@srl.caltech.edu
[4] Center for Astrophysics and Space Astronomy, University of Colorado, Boulder, CO 80309, USA; christopher.moore-1@colorado.edu
[5] Department of Astronomy, University of Maryland, College Park, MD 20742, USA; share@astro.umd.edu
[6] Naval Research Laboratory, Code 7663, Washington, DC 20375, USA; vourlidas@nrl.navy.mil
[7] Space Sciences Laboratory, University of California, Berkeley, CA 94720, USA; welsch@ssl.berkeley.edu

ABSTRACT

We have evaluated the energetics of 38 solar eruptive events observed by a variety of spacecraft instruments between 2002 February and 2006 December, as accurately as the observations allow. The measured energetic components include: (1) the radiated energy in the *Geostationary Operational Environmental Satellite* 1–8 Å band, (2) the total energy radiated from the soft X-ray (SXR) emitting plasma, (3) the peak energy in the SXR-emitting plasma, (4) the bolometric radiated energy over the full duration of the event, (5) the energy in flare-accelerated electrons above 20 keV and in flare-accelerated ions above 1 MeV, (6) the kinetic and potential energies of the coronal mass ejection (CME), (7) the energy in solar energetic particles (SEPs) observed in interplanetary space, and (8) the amount of free (non-potential) magnetic energy estimated to be available in the pertinent active region. Major conclusions include: (1) the energy radiated by the SXR-emitting plasma exceeds, by about half an order of magnitude, the peak energy content of the thermal plasma that produces this radiation; (2) the energy content in flare-accelerated electrons and ions is sufficient to supply the bolometric energy radiated across all wavelengths throughout the event; (3) the energy contents of flare-accelerated electrons and ions are comparable; (4) the energy in SEPs is typically a few percent of the CME kinetic energy (measured in the rest frame of the solar wind); and (5) the available magnetic energy is sufficient to power the CME, the flare-accelerated particles, and the hot thermal plasma.

Key words: Sun: activity – Sun: coronal mass ejections (CMEs) – Sun: flares – Sun: particle emission –
Sun: X-rays, gamma rays

1. INTRODUCTION

Solar eruptive events (SEEs), which are comprised of flares and associated coronal mass ejections (CMEs), are the most energetic occurrences in the solar system. Over a period of tens of seconds to minutes, they can convert upward of 10^{32} erg of energy carried in non-potential, current-carrying magnetic fields into accelerated particles, heated plasma, and ejected solar material.

While the overall energy involved in a large SEE is not in serious doubt, its partition among its component parts has so far been estimated only for a few events. In this paper, we provide the first statistical analysis of energy partition throughout the various manifestations of an SEE, for 38 large events. We provide this information not only to establish "typical" ratios of the energy in various components of the event, but also to provide some idea of the range over which such ratios extend, and we especially point out events in which the strength of one component or another appears to lie outside the norm. We offer this analysis with the goal of providing useful constraints for modelers of the energy release process(es) involved.

This paper grew out of the energetics working group at the meeting on "Solar Activity during the onset of Solar Cycle 24" held in Napa, CA, from 2008 December 8–12. It is a continuation of the work begun at the Taos *ACE/RHESSI/WIND* joint workshop in 2003 that led to the works of Emslie et al. (2004, 2005). These papers provided the first detailed analysis of most of the components of two well-observed SEEs (the *GOES* X1.5 event on 2002 April 21 and the X4.8 flare event

of 2002 July 23), including the energies in thermal plasma, flare-accelerated electrons and ions, associated CME, and solar energetic particles (SEPs). Emslie et al. (2004) showed that, for the two events in question, the energy in the magnetic field was sufficient to power the thermal soft X-ray (SXR) emitting plasma, the flare-accelerated electrons and protons, and the kinetic energy in the CME, and they also provided order-of-magnitude estimates of the partition of the energy among these components. Subsequently, Emslie et al. (2005) also considered the energy in the optical and EUV continua, and they cautioned that, due to the transfer of one energy component to another (e.g., flare-accelerated electrons → thermal plasma → SXR emission), care must be taken in summing energetic components to arrive at the total energy released in an SEE. The present paper is also motivated by the work of Mewaldt et al. (2008b), which was the first to address the ratio of two energetic components (the CME energy in the rest frame of the solar wind and the energy in SEPs) for a statistically significant number of well-observed events.

The basic objective of the paper is to conduct a statistical study of the energy partition into different components for many of the larger SEEs observed during the previous maximum of solar activity, particularly during the period 2002 February–2006 December, the first five years of observations by the *Ramaty High Energy Solar Spectroscopic Imager* (*RHESSI*; Lin et al. 2002). The intent is to apply previously proven techniques to determining the global energetics of many more events than the two studied by Emslie et al. (2004, 2005), and, where possible, to apply new techniques to improve the energy estimates.

Our energy estimates come from a wide variety of observations: CME kinetic and potential energies from the Large Angle and Spectrometric COronagraph (LASCO; Brueckner et al. 1995) instrument on the *Solar and Heliospheric Observatory* (*SOHO*); energy in flare-accelerated charged particles inferred from the hard X-rays and gamma rays observed by *RHESSI*; energy contained in the SXR-emitting hot plasma from the *Geostationary Operational Environmental Satellites* (*GOESs*) and *RHESSI*; energy in SEPs from the suite of instruments on the *Advanced Composition Explorer* (*ACE*) and from *GOES*, *SOHO*, the *Solar Anomalous and Magnetospheric Particle EXplorer* (*SAMPEX*), and the *Solar TErrestrial RElations Observatory* (*STEREO*); and total radiated energy from the Total Irradiance Monitor (TIM; Kopp & Lawrence 2005) on the *SOlar Radiation and Climate Experiment* (*SORCE*). For weaker events, or where total irradiance measurements are not available, the Flare Irradiance Spectral Model (FISM; Chamberlin et al. 2007, 2008) was used to provide estimates of the bolometric output of a flare based on other measurements.

In Section 2, we present the events studied and review the techniques used to estimate the different component energies of each event. In Section 3, we present a series of scatter plots of one energy component against another. While the uncertainties on the individual energy estimates are typically large (often an order of magnitude or greater), these scatter plots, because of the relatively large number of events they contain, nevertheless allow some general conclusions to be reached (Section 4) about how the energy is partitioned. The spread in the values for the different energy components also gives an idea of the uncertainties in the measured parameters and the range of flare intensities of the selected events. These plots also allow for the identification of a few "outlier" events (Section 5) that indicate either larger measurement uncertainties or distinctly different energy partitioning for those events. We summarize the results in Section 6, which also provides suggestions for future work.

2. COMPONENT ENERGIES OF THE SOLAR ERUPTIVE EVENTS

The events studied are listed in Table 1. They include the largest SEP events observed after 2002 February, when *RHESSI* was launched, excluding those events beyond the west limb (for which no reliable active region identification can be made) and those events located from E60° to E90° (for which the evaluation of the SEP energy is highly uncertain—see Section 2.7). They also include the two events studied by Emslie et al. (2004), which appear as Events 2 and 6 in Table 1. Additional events include all flares for which *RHESSI* detected significant ($>4\sigma$) emission in the 2.223 MeV neutron-capture gamma-ray line (Shih 2009; Shih et al. 2009). This, plus the inclusion of an intriguing behind-the-limb event with a strong CME on 2002 July 20 (Event 5 in Table 1), resulted in a total of 38 events for study. As permitted by the available data, estimates were made of the following energies for each of the 38 events.

1. Radiated energy in the *GOES* 1–8 Å band.
2. Total radiated energy from the SXR-emitting plasma.
3. Total (bolometric) radiated output.
4. Peak thermal energy of the SXR-emitting plasma.
5. Energy in flare-accelerated electrons.
6. Energy in flare-accelerated ions.
7. CME kinetic energy in the rest frame of the Sun.
8. CME kinetic energy in the solar wind rest frame.

9. CME gravitational potential energy.
10. Energy in SEPs.
11. Free (non-potential) magnetic energy in the active region.

It is important to keep in mind the differences among the first four items on this list. They are all related, but are included separately since they can each be estimated independently, and indeed relatively straightforwardly, from the available measurements, and since collectively they provide significant information on the thermal energy of each flare, how it is distributed in temperature, and when it is generated and released. Further details on these four items are provided in Sections 2.1–2.3. Broadly speaking, the first item is the energy radiated in the narrow *GOES* band from 1 to 8 Å, obtained directly from background-subtracted data (Section 2.1). The second is the energy radiated over *all* wavelengths (including the 1–8 Å band) from the hot SXR-emitting plasma and is a quantity inferred from the plasma parameters (emission measure and temperature) revealed by the *GOES* 1–8 Å measurements. The third item is the total energy radiated over all wavelengths from *all* components of the flare at *all* temperatures (including that from the SXR-emitting plasma); in some cases this is directly observed and in some cases inferred from modeling of the emission in select wavelength ranges—see Section 2.2. The fourth item does not specify a radiated energy at all, but rather the peak thermal energy content of the hot SXR-emitting plasma; this quantity is inferred (Section 2.3) from the parameters of spectroscopic fits to *RHESSI* data. It is important to realize (Emslie et al. 2005) that these four components are not separate flare energy components and therefore cannot be summed together to obtain a total flare thermal energy.

We have not evaluated energy losses from the SXR-emitting plasma by thermal conduction. However, we would note that conductive transfer of thermal energy from hot SXR-emitting plasma into the relatively cool chromospheric plasma will generally result in the thermal energy content of the hot SXR-emitting plasma being quite effectively transported to, and ultimately radiated away by, such relatively cool plasma, one contribution to the total (bolometric) radiated output—the third item on the list. Further, for the events considered here there is little observational data available on the energy contained in turbulence and directed mass motions of thermal plasma, components that may well contain energies comparable to the thermal energy of the SXR-emitting plasma (see, e.g., Doschek et al. 1992).

The data on all the component energies are summarized in Table 1. *GOES* SXR data are available for all the events. However, because of missing or inadequate data or limited instrument sensitivities, definitive energy estimates for all the energy components listed above are available for only six events (Events 13, 14, 20, 23, 25, and 38). As mentioned above, Event 5 was located behind the limb; thus only a "plausible" magnetic energy estimate (not included in Table 1) could be obtained from observations of the most likely responsible active region once it had moved onto the solar disk, and the listed radiated energies are lower limits.

2.1. Radiated Energy from Hot Plasma

For each event, we estimated the time-integrated SXR and total radiated energies from the hot SXR-emitting plasma—the columns labeled "SXR" and "T-rad," respectively, in Table 1. Fluxes in W m^{-2} for the 1–8 Å and 0.5–4 Å bands are provided by one of NOAA *GOES* satellites every 3 s. The total emission

Table 1
Event List with Component Energies ($\times 10^{30}$ erg)

No.	Date[a]	Time[b]	Class	SXR[c]	T-rad[d]	Bol[e]	Peak[f]	Elec[g]	Ion[h]	KE[i]	SW[j]	PE[k]	SEP[l]	Mag[m]
1	02/02/20	05:52	M5.1	0.043	1.2	13	...	...	...	17	5.6	6.3	0.13	1200
2	02/04/21	00:43	X1.5	1.2	38	150	13	20	...	230	160	5.0	23	660
3	02/05/22	03:18	C5.0	0.048	5.6	9	...	...	...	84	45	10	2.7	260
4	02/07/15	19:59	X3.0	0.31	6.4	44	>2.2	>3.6	...	160	76	10	3.8	1500
5	02/07/20	21:04	X3.3[n]	>1.5	>26	>210	...	...	...	260	170	...	...	...
6	02/07/23	00:18	X4.8	1.2	19	150	2.5	32	39	260	150	20	<30	2000
7	02/08/24	00:49	X3.1	1.1	24	160	5.9	11	...	210	130	16	3.9	2500
8	02/11/09	13:08	M4.6	0.11	5.0	8	1.3	60	...	180	110	20	0.51	550
9	03/05/27	22:56	X1.4	0.16	3.6	16	2.8	7.4	0.19	...	...	...	...	260
10	03/06/17	22:27	M6.9	0.21	4.6	17	2.4	4.6	6.7	...	...	...	...	140
11	03/10/26	17:21	X1.2	1.2	31	88	...	...	...	240	130	32	0.75	1700
12	03/10/28	09:51	X17	4.4	68	362[o]	>19	>56	>190	1200	850	63	43	2900
13	03/10/29	20:37	X10	1.9	31	137[o]	11	110	30	340	220	25	9.7	2900
14	03/11/02	17:03	X8.3	1.8	24	130	9.3	130	68	270	200	10	9.3	2800
15	03/11/03	09:43	X3.9	1.1	17	97	2.4	120	3.1	...	...	...	...	780
16	03/11/04	19:29	X28	4.8	72	426[o]	>3.1	>21	...	610	410	25	5.3	2800
17	04/07/15	18:15	X1.6	0.16	4.1	8	0.93	42	<0.1	...	...	...	...	820
18	04/07/25	05:39	M7.1	0.069	1.3	10	...	...	...	...	...	...	2.9	2300
19	04/11/07	15:42	X2.0	0.32	5.0	56	3.0	43	...	220	130	25	4.2	610
20	04/11/10	01:59	X2.5	0.32	7.7	15	2.0	20	3.4	230	180	16	2.4	610
21	05/01/15	00:22	X1.2	0.23	4.7	23	5.0	32	...	...	...	...	...	1500
22	05/01/15	22:25	X2.6	1.3	22	78	7.1	63	15	730	540	...	...	1600
23	05/01/17	06:59	X3.8	1.8	34	150	17	48	13	1000	730	50	11	1600
24	05/01/19	08:03	X1.3	0.43	7.0	54	5.9	82	29	...	...	...	...	1600
25	05/01/20	06:36	X7.1	2.9	43	150	10	25	120	15–79	7.8–61	2.0	7.8	1600
26	05/05/13	16:13	M8.0	0.44	14	49	3.1	13	...	39	22	4.0	7.3	400
27	05/07/14	10:16	X1.2	0.64	12	87	4.3	24	...	100	66	6.3	2.9	310
28	05/07/27	04:33	M3.7	0.16	4.5	30	1.3	12	...	100	62	10	...	310
29	05/08/22	16:46	M5.6	0.34	9.8	35	3.2	6.3	...	110	76	10	6.4	390
30	05/08/25	04:31	M6.4	0.050	1.2	11	1.1	16	<1.9	...	...	...	...	110
31	05/09/07	17:17	X17	4.9	68	322[o]	>5.6	>10	>0.7	...	...	...	...	1400
32	05/09/09	19:13	X6.2	3.1	44	250	>7.9	>120	>1.7	...	...	...	...	1300
33	05/09/10	21:30	X2.1	0.99	17	82	6.0	13	1.0	...	...	...	...	1300
34	05/09/13	19:19	X1.5	1.1	25	85	...	...	...	330	200	32	3.0	1400
35	05/09/13	23:15	X1.7	0.23	4.7	21	2.3	32	<0.1	...	...	...	...	1400
36	06/12/05	10:18	X9.0	1.4	19	92	>5.1	>360	>4.5	...	...	...	...	400
37	06/12/06	18:29	X6.5	1.1	18	59[o]	6.8	40	36	...	...	...	...	410
38	06/12/13	02:14	X3.0	1.1	17	75	4.8	13	14	74	44	6.3	3.2	570

Notes.
[a] In yy/mm/dd format.
[b] *GOES* start time (UT).
[c] Radiated energy in the *GOES* 1–8 Å band.
[d] Total radiated energy from the SXR-emitting plasma.
[e] Bolometric radiated energy.
[f] Peak thermal energy of the SXR-emitting plasma.
[g] Energy in flare-accelerated electrons.
[h] Energy in flare-accelerated ions.
[i] CME kinetic energy in the rest frame of the Sun.
[j] CME kinetic energy in the solar wind rest frame.
[k] CME gravitational potential energy.
[l] Energy in SEPs.
[m] Non-potential magnetic energy in the active region.
[n] Behind-the-limb event.
[o] Bolometric irradiance directly measured with TIM—see Table 2.

in the 1–8 Å band ("SXR") is obtained simply by summing the background-subtracted fluxes over the duration of the flare, from the *GOES* start time (given by NOAA and listed in Table 1) to the time when the flux had decreased to 10% of the peak value. The background that was subtracted was taken as the lowest flux in the hour or so before and/or after the flare.

To calculate the radiated energy from the hot plasma, we used the measured *GOES* SXR fluxes in a manner similar to that described in Emslie et al. (2004), specifically using the IDL *GOES* Workbench available in SolarSoftware (SSW). This allows us to obtain a consistent set of values for all events since *GOES*, unlike *RHESSI*, has full coverage for all events. This calculation assumes that the hot plasma at any given time is isothermal; the temperature and emission measure are calculated from the two-channel *GOES* data using the relations given by White et al. (2005). Using the emission measure

Table 2
TIM and FISM Bolometric Energies (10^{30} erg)

Event	Date	TIM				FISM	Difference
No.		Total[a]	Uncertainty[a]	Revised Estimate	Corrected[b]	Corrected[b]	(TIM − FISM)/TIM
12	2003 Oct 28	600	39%	362	362	310	14%
13	2003 Oct 29	240	86%	137	137	128	7%
16	2003 Nov 4	260	65%	142	426	447	−5%
31	2005 Sep 7	300	71%	150	322	266	17%
37	2006 Dec 6	. . .	. . .	46[c]	59	82	−39%

Notes.
[a] Woods et al. (2006).
[b] Corrected for limb darkening.
[c] C. S. Moore et al. (2012, in preparation).

and temperature thus inferred, and the optically thin radiation loss rate versus temperature function (for coronal abundances and Mazzotta et al. 1998 ionization equilibria) taken from the CHIANTI database (Dere et al. 1997, 2009), we used the IDL procedure *rad_loss*, available in SSW, to calculate, for each 3 s time interval, the energy radiated from the SXR-emitting plasma over all wavelengths. Finally, we summed the radiated energies over the duration of the flare (from the *GOES* start time until the 1–8 Å flux decreased to 10% of its peak value) to produce the total radiated energy given in the column labeled "T-rad" in Table 1. Significant energy could be radiated after this nominal end of the flare, particularly if there is a "second phase" that, according to Woods et al. (2011) and Su et al. (2012), can release an amount of energy that is similar to that released in the initial phase. Generally, however, the values quoted in Table 1 should include more than 50% of the energy radiated by the SXR-emitting plasma.

2.2. Bolometric Irradiance

Estimates of the bolometric irradiance, the total energy radiated from the flare integrated across the entire solar spectrum, for each of the events are provided in the column labeled "Bol" in Table 1. For five of the events listed in Table 1, the bolometric irradiance was measured directly by the TIM (Kopp & Lawrence 2005) on board *SORCE* as an increase in the total solar irradiance above the (highly variable) pre- and post-flare background levels. Total flare irradiance values were reported in this manner for Events 12, 13, 16, and 31 by Woods et al. (2006), and the bolometric irradiance for Event 37 will be reported by C. S. Moore et al. (2012, in preparation). Both previously published values and revised estimates made for this paper are listed in Table 2. A final correction factor (see Table 2) was then applied to allow for limb-darkening absorption when the path to the observer becomes optically thick at some wavelengths; the value of this factor can be up to ∼3.0—see Equation (2) in Woods et al. (2006).

To complement these direct measurements and so provide a consistent set of bolometric values for all of the events in Table 1, estimates from the FISM (Chamberlin et al. 2007, 2008) were used, with various assumptions and corrections as described below. FISM is an empirical model that provides estimates of the total amount of solar radiated energy over a broad wavelength range from 1 to 1900 Å and over a wide range of timescales from seconds to years. It uses measurements in this wavelength range from the Solar EUV Experiment (SEE; Woods et al. 2005) on the *Thermosphere Ionosphere Mesosphere Energetics and Dynamics* (*TIMED*) satellite and the SOLar-STellar Irradiance Comparison Experiment

(SOLSTICE; Rottman et al. 1993) on the *Upper Atmosphere Research Satellite*.

For the relatively rapid *GOES* 1–8 Å SXR flux variations that occur during a solar flare, different empirical factors appropriate to the rise and decay phases of the flare, respectively, are used to relate the SXR flux to the total radiated energy during those phases. Various daily proxies are also used to represent the more gradual variations in solar irradiance due to active region evolution, solar rotation, and the solar cycle. The daily pre-flare irradiance spectrum is subtracted from each value to get the radiated energy from the flare alone, and this is then integrated over the duration of the *GOES* flare to get the total radiated energy in erg cm^{-2} at the detector. Then, assuming uniform radiation over 2π steradians, the total radiated energy from the flare in the 1–1900 Å wavelength range can be calculated, with 1 minute cadence.

The 1–1900 Å solar irradiance is converted to total radiated energy over all wavelengths (the bolometric irradiance) by multiplying by an empirical conversion factor of 2.42 ± 0.31, determined by comparing the 1–1900 Å solar irradiance with the absolute bolometric intensity for the five flares for which the latter could be measured directly (see Table 2).

The uncertainties on the calculated values of the bolometric irradiance listed in Tables 1 and 2 are made up of several parts. The dominant uncertainty comes from the TIM measurements themselves and is due to the variations in the total solar irradiance of the non-flaring Sun. Other contributions to the overall uncertainty are the errors on the FISM estimates of the 1–1900 Å flux, the conversion from UV irradiance to total solar irradiance, and the limb-darkening correction. The overall uncertainty on the calculated values is ± ∼70% for those events that are near disk center and ± ∼90% for the near-limb events.[8]

2.3. Peak Thermal Energy Content of the Hot Plasma

The peak thermal energy content of the SXR-emitting plasma (the column labeled "Peak" in Table 1) was determined from *RHESSI* imaging spectroscopy data. We first fit the observed *RHESSI* hard X-ray spectra with the sum of a single-temperature Maxwellian plus the form expected from a double-power-law electron spectrum (Equation (2) in Section 2.4). The fit parameters appropriate to both thermal and nonthermal components were determined for each time interval using the forward-fitting method implemented in the OSPEX software package available in SSW. The temperatures and emission measures obtained from

---

[8] Because the conversion of the FISM radiated energy to bolometric energy is based on the five events measured directly with TIM, the bolometric energies for these five events derived from the FISM estimate differ (after correcting for limb darkening) by less than 40% from the directly measured values.

RHESSI in this way tend to agree closely with the corresponding values obtained from the standard *GOES* data analysis discussed in Section 2.1. However, somewhat higher temperatures can be obtained because of the *RHESSI* coverage to higher energies; indeed, superhot components with reported temperatures as high as ~50 MK may exist in some flares and are not accurately reflected in the *GOES* thermal analysis (Lin et al. 1981; Caspi 2010; Caspi & Lin 2010). The thermal function included the line-plus-continuum components determined using CHIANTI, again with coronal abundances and Mazzotta et al. (1998) ionization equilibria. From these fits, the average temperature T_0 (K) and emission measure EM $= \int n_e^2 \, dV$ (cm^{-3}) of the thermal plasma were determined every 20 s throughout the flare. (Here n_e is the electron density (cm^{-3}) and V is the emitting volume (cm^3).)

The thermal energy content $U_{\rm th}$ of the plasma can be calculated from the expression (e.g., de Jager et al. 1986)

$$U_{\rm th} = 3 \, n_e \, k T_0 \, f \, V_{\rm ap} \simeq 4.14 \times 10^{-16} \, T_0 \, \sqrt{{\rm EM} \times f \, V_{\rm ap}} \ {\rm erg},$$
(1)

where k is Boltzmann's constant, f is the volumetric filling factor, and $V_{\rm ap}$ is the apparent volume of the SXR source. Starting in 2003, SXR images are also available from the *GOES* Soft X-ray Imagers (SXIs; Lemen et al. 2004; Pizzo et al. 2005); such images could be used to provide estimates of $V_{\rm ap}$, as described in Emslie et al. (2004). However, both for consistency with the earlier analysis of Emslie et al. (2004, which analyzed events that occurred in 2002, prior to the SXI deployment), and since the parameters EM and T_0 in Equation (1) are deduced from *RHESSI* data, we have chosen to use estimates of $V_{\rm ap}$ that are deduced from *RHESSI* images, made using the 3σ clean method of Dennis & Pernak (2009). We further take f to be unity, consistent with Emslie et al. (2004) and further justified by the recent work of Guo et al. (2012), who used hard X-ray imaging spectroscopy data of 22 extended-loop events to derive a (logarithmic) mean filling factor $f = 0.20 \times/\div 3.9$ (1σ standard error).

The peak energy values listed in Table 1 are the highest values of $U_{\rm th}$ obtained from this analysis, usually at or near the time of the peak *GOES* flux.

2.4. Flare-accelerated Electrons

The energies in flare-accelerated electrons are listed in the column labeled "Elec" in Table 1. They were determined by using the OSPEX algorithm to fit a combined isothermal-plus-nonthermal function to the measured *RHESSI* spatially integrated X-ray spectra. The nonthermal component was assumed to be bremsstrahlung from energetic electrons with an injected spectrum $F_0(E_0)$ (electrons cm^{-2} s^{-1} keV^{-1}) in the form of a broken power law:

$$F_0(E_0) = A \begin{cases} 0, & E_0 < E_{\rm min} \\ (E_0/E_p)^{-\delta_1}, & E_{\rm min} \leqslant E_0 < E_b \\ (E_0/E_p)^{-\delta_2}(E_b/E_p)^{\delta_2-\delta_1}, & E_b \leqslant E_0 < E_{\rm max} \\ 0, & E_{\rm max} \leqslant E_0. \end{cases}$$
(2)

The seven parameters of this model spectrum are the normalization parameter A, the low- and high-energy cutoffs $E_{\rm min}$ and $E_{\rm max}$, the break energy E_b, and the power-law indices δ_1 and δ_2 below and above the break energy, respectively. The (arbitrary) value of the pivot energy E_p was fixed at 50 keV. Also, the high-energy cutoff $E_{\rm max}$ was fixed at 30 MeV, an energy so

high above the energy range of interest ($\lesssim$500 keV) that it has a negligible effect on the calculated X-ray spectrum and so is equivalent to having no high-energy cutoff at all.

The OSPEX analysis uses a forward-fitting procedure that starts by dividing the flare into multiple time intervals—here we used 20 s intervals. For each interval, the function *thick2* in SSW is used with a set of starting parameters for the electron spectrum (2) used to calculate the X-ray photon spectrum, assuming electron–ion bremsstrahlung in a thick target that is "cold" in the sense that the ambient electrons have a mean energy kT that is significantly lower than the lowest energy of the accelerated electrons. In general, consideration must also be given to the ionization state of the target, since the bremsstrahlung efficiency is a factor of ~3 times higher for a fully ionized plasma than for an un-ionized gas (Brown 1973; Kontar et al. 2003). However, since most of the beam energy is in the lower energy electrons that stop higher in the corona, we used parameters appropriate for a fully ionized plasma to calculate the total nonthermal energy. A more refined calculation is possible using the procedure outlined by Kontar et al. (2002) and Su et al. (2011), but no significant difference is expected in the resulting total energy in electrons above $E_{\rm min}$.

The resulting photon spectrum is then folded through the detector response matrix to generate a count-rate spectrum, which is added to the count-rate spectrum calculated for the thermal spectrum discussed in Section 2.1. Then, through an iterative procedure, we find best-fit values of the parameters describing the electron spectrum (2) by minimizing the χ^2 statistic between the calculated and the measured background-subtracted count spectra. The total energy U_e in electrons for a given event is then computed by integrating the best-fit electron energy spectrum above $E_{\rm min}$ for each time interval and summing the results over the duration of the flare, resulting in the values listed in the column labeled "Elec" in Table 1.

In order to obtain the most reliable spectral fits to the *RHESSI* data and thus better evaluate the uncertainties in the calculated values of U_e, we chose to use data from just one of *RHESSI*'s nine detectors—detector 4. This particular detector has good energy resolution and sensitivity, which allowed us to apply the most up-to-date corrections for energy resolution and calibration, photospheric albedo, pulse pile-up, and background subtraction that are available with the current analysis software. For the large events studied, the count rates were sufficiently high that selecting just a single detector did not seriously degrade the spectroscopic capability up to the photon energies required to determine the parameters of interest. Milligan & Dennis (2009) have shown that similar best-fit parameter values are determined using different individual detectors (detectors 1, 3, 4, 5, 6, and 9 in their case), which leads to an estimate of the systematic uncertainties in the calculated total energy in electrons of ~20%. This is negligible compared to the uncertainty arising from the difficulty in establishing the value of the low-energy cutoff energy $E_{\rm min}$, an uncertainty that arises because the thermal emission generally dominates the low-energy part of the X-ray photon spectrum up to energies where the effects of a cutoff in the electron spectrum might be detectable. We used the largest value of $E_{\rm min}$ that still gave an acceptable fit (reduced $\chi^2 \simeq 1$). As a result, the values of U_e listed in Table 1 are lower limits to the energy in the nonthermal electrons. Furthermore, because of the steep form of the electron spectra ($\delta_1 \gtrsim 4$), these values are particularly sensitive to $E_{\rm min}$, so that the energies in flare-accelerated electrons could be up to an order of magnitude higher than those reported in Table 1.

2.5. Flare-accelerated Ions

The energies in flare-accelerated ions with energies above 1 MeV are listed in the column labeled "Ion" in Table 1. In order to provide a consistent set of values for as many events as possible, the energies were estimated solely from *RHESSI* measurements of the fluence (time integral of the flux, photons cm^{-2}) in the 2.223 MeV neutron-capture gamma-ray line. Our sample of events is primarily based on the studies of Shih (2009) and Shih et al. (2009), who analyzed *RHESSI* flares from 2002 to 2005 that had either 2.223 MeV line emission and/or >0.3 MeV electron bremsstrahlung continuum emission. Of those flares, energies are included only for those that have >2σ detections of that line, and further only as 4σ upper limits if below a 4σ detection. We also include three additional flares that occurred in 2006 (Events 36–38). We chose a lower energy threshold of 1 MeV because the production of detected nuclear gamma-ray lines from elements such as ^{20}Ne begins at energies as low as $\sim$3 MeV, and it is therefore evident that the ion spectrum extends down to $\sim$1 MeV, at least in a few large events (Ramaty et al. 1995; Ramaty & Mandzhavidze 2000). The spectral shape is essentially unknown below 1 MeV.

In order to estimate the energy in ions from the 2.223 MeV line fluences, the following steps were taken. The measured fluences of the line were first corrected for attenuation in the solar atmosphere assuming a given depth of production of the photons (Hua & Lingenfelter 1987) and allowing for the flare position on the solar disk. The corrected fluence values were then converted to the proton energy above 30 MeV using conversion factors given by Murphy et al. (2007) and Shih (2009). The 30 MeV threshold was used at this stage in the analysis because the 2.223 MeV line is produced by ions with energies $\gtrsim$20 MeV nucleon^{-1}, so that the conversion factors are less dependent on the assumed power-law index of the proton spectrum.

In order to estimate the energy in protons above 1 MeV, an extrapolation is required over one-and-a-half orders of magnitude in proton energy, so that the inferred energy above 1 MeV depends critically on the spectral index used in this extrapolation. For the largest *RHESSI* flares, where multiple types of ion-associated gamma-ray emission can be detected and fitted simultaneously, the ion power-law spectral indices are found to be typically in the range 3–5, a range of indices consistent with that found in a study of flares observed by the Gamma-Ray Spectrometer on the *Solar Maximum Mission* (Ramaty et al. 1996). Consequently, for the purposes of estimating the total energy in protons, we have assumed a power-law proton spectrum with a single spectral index of 4 that extends down to a lower cutoff energy of 1 MeV. Because of the long "lever arm" associated with this extrapolation, an uncertainty in the spectral index of $\pm$1 corresponds to an uncertainty in the total energy content above 1 MeV of about $\pm$1.5 orders of magnitude.

Even under the assumption that the spectra for the various types of ions have the same spectral index and low-energy cutoff, the energy content will also depend on the accelerated particle composition. The ratio of the energy content in all ions (protons plus α-particles and heavier nuclei) to the energy in protons can vary between $\sim$2 and $\sim$6; here we assume that the energy in flare-accelerated ions is three times the energy content in flare-accelerated protons.

For a number of the events, the total energy content of ions listed in Table 1 is a lower limit because *RHESSI* did not see the complete time history as the result of spacecraft night or passage through the South Atlantic Anomaly. In addition, there can be other complications that affect the observation or interpretation of the neutron-capture line. The affected events are as follows.

1. *Event 12. RHESSI* missed a significant fraction of the neutron-capture line emission, including the peak, as shown by observations of this flare by *International Gamma-Ray Astrophysics Laboratory* (Kiener et al. 2006).
2. *Event 31: RHESSI* observed only $\sim$2 minutes of a significantly longer impulsive phase. Furthermore, the level of atmospheric attenuation is very uncertain due to this flare's large heliocentric angle, so we use a conservative angle of 80° to determine the correction factor.
3. *Events 32 and 37. RHESSI* missed the peak of the impulsive emission, and thus possibly a significant fraction of the total emission.
4. *Event 36. RHESSI* missed some fraction of the 2.223 MeV emission as it was just coming out of Earth shadow. *RHESSI* observations started at 10:31 UT and the *GOES* X-ray flare started at $\sim$10:19 UT.
5. *Events 14, 15, 22, 33, and 38. RHESSI* likely missed a small fraction of the neutron-capture line emission late in the flare. However, this missing energy is smaller than the other uncertainties in the energy estimates discussed above.
6. *Events 36–38.* By 2006 December, *RHESSI*'s detectors had reduced gamma-ray sensitivity resulting from accumulated radiation damage, a reduction that is difficult to estimate.

2.6. Coronal Mass Ejection

The CME kinetic energies, both in the rest frame of the Sun and in that of the solar wind (for comparison with the SEP energies—see Section 3.6), are listed in the columns labeled "KE" and "SW," respectively, of Table 1. The gravitational potential energies of the CMEs are listed in the column labeled "PE." These CME energies were estimated from calibrated LASCO images using the procedure detailed in Vourlidas et al. (2010, 2011).

Briefly, this procedure consists of the following steps. First, we selected two LASCO images, one containing the CME and the other taken before the event as close in time as possible to the flare with no disturbances or ejecta over the path of the subsequent CME. Next, the images were calibrated (in units of mean solar brightness) and the pre-event image was subtracted from the CME image. The excess brightness revealed by this subtracted image is due to Thomson scattering of photospheric radiation from the excess mass in the CME. This excess brightness can therefore be converted to excess mass of the CME under the usual assumptions that (1) all of the CME mass is concentrated on the plane of the sky and (2) the CME material consists of 90% H and 10% He (Poland et al. 1981; Vourlidas et al. 2000, 2010). We used the first assumption because the true three-dimensional distribution of the CME mass along the line of sight (LOS) is unknown. The second assumption represents an "average" coronal composition, since we do not know the height at which the bulk of the CME material originates (other than that it is coronal).

These assumptions together result in a lower limit for the mass. The uncertainty in the CME mass becomes more significant as the central angle and/or spread of a given CME departs significantly from the plane of the sky. The mass underestimation is about a factor of two for CMEs that are $\lesssim$40° from the sky plane (Vourlidas et al. 2010).

Other uncertainties in this procedure include exposure time variations between event and pre-event images, improper

vignetting correction, solar rotation effects, and the presence of stars in the field of view. Fortunately, such uncertainties can be minimized to a level that is well below that of other factors through proper calibration and careful choice of event and pre-event images.

After obtaining a series of excess masses of the CME as a function of time, we can compute both the total mass of the CME and the position and projected velocity, both for the leading edge and for the center of mass of the CME. From the mass m, position r, and velocity V, we can straightforwardly estimate the total kinetic ($U_K = (1/2)mV^2$) and potential ($U_\Phi = GM_\odot m(R_\odot^{-1} - r^{-1})$) energies (here G is the Newtonian gravitational constant and $M_\odot$ and $R_\odot$ are the solar mass and radius, respectively). These values are again lower bounds since both the mass and the speed are projected quantities. Vourlidas et al. (2010) estimate that, for CMEs that are far away from the sky plane and that have relatively small widths, the kinetic energy could be as much as a factor of eight times larger than the values derived above; similarly the potential energy could be as much as twice as large for such events. However, for the majority of events, the uncertainties on the quoted energies are within a factor of two. To obtain the kinetic energy in the solar wind rest frame (as an estimate of the energy available for shock acceleration of SEPs; see Section 3.6), we simply subtracted 400 km s^{-1} from the measured CME speed and recomputed the kinetic energy using the speed in this new reference frame.

2.7. Solar Energetic Particles (SEPs)

For the majority of the events studied, it is likely that the interplanetary SEPs in the events studied are accelerated by CME-driven shocks. (A possible exception is the 2002 February 20 event, where particles directly accelerated in the flare could dominate; see Chollet et al. 2010.) The energy content of the accelerated SEPs, particularly when compared to the kinetic energy of the CME in the solar wind rest frame, is therefore an important measure of the efficiency of SEP production by the CME.

The energy content of SEPs that escape into interplanetary space has been estimated by measuring the energy spectra of electrons from ~0.035 to ~8 MeV, protons from ~0.05 to ~400 MeV nucleon^{-1}, and abundant heavier ions from ~0.05 to ~100 MeV nucleon^{-1}. Estimates were made in a number of large events from Solar Cycle 23 using a combination of nine separate instruments. The proton spectra are based on data from the Ultra-Low Energy Isotope Spectrometer (ULEIS; Mason et al. 1998) and the Electron, Proton, and Alpha Monitor (EPAM; Gold et al. 1998) on *ACE*; from the Proton/Electron Telescope (PET; Cook et al. 1993) on *SAMPEX*; and from the Energetic Particle Sensors (EPS; Onsager et al. 1996) on NOAA's *GOES-8* and *GOES-11* satellites. Spectra of helium and heavier ions were measured by the Solar Isotope Spectrometer (SIS; Stone et al. 1998) on *ACE* and by ULEIS. Also used for the 2006 events were two *STEREO* instruments, the Low Energy Telescope (LET; Mewaldt et al. 2008a) and High Energy Telescope (HET; von Rosenvinge et al. 2008). Electron measurements were provided by *ACE*/EPAM, *SAMPEX*/PET, and by the Electron Proton Helium INstrument (EPHIN; Müller-Mellin et al. 1995) instrument on *SOHO*.

For 11 of these events, the energy spectra of H, He, and abundant heavier ions were all fitted with common spectral forms that include the double-power-law function of Band et al. (1993) and the Ellison & Ramaty (1985) spectrum—a power law with an exponential cutoff. Examples of energy spectra and both functional forms are given in Mewaldt et al. (2005, 2012) and Cohen et al. (2005). For the remainder of the events, the proton energy spectra were fitted and the contributions of He and heavier ions were estimated using element abundances measured for these events by ULEIS and SIS. The electron contribution was measured in each of the individual events using either EPAM and PET, or EPAM and EPHIN.

For all of the fluence measurements described above, the instruments were located near Earth. As in Emslie et al. (2004), we used the measured near-Earth fluence spectra, typically integrated over 3–5 days, to estimate the energy cm^{-2} that escaped beyond 1 AU in the form of SEPs. To obtain this estimate, Emslie et al. (2004) corrected for the fact that SEPs can scatter back and forth across 1 AU (providing multiple opportunities to be measured) using correction factors based on simulations by J. Giacalone (2002, private communication). A similar approach was followed in analyzing the "Halloween" events (Mewaldt et al. 2005) and in a subsequent survey of 17 events (Mewaldt 2006). Mewaldt et al. (2008b) improved on these estimates in a study of 23 SEP events from 1997 to 2005 by correcting for the fact that SEPs also lose energy as they scatter on the diverging interplanetary magnetic field.

For this work, we corrected for both multiple 1 AU crossings and energy loss using new simulations by Chollet et al. (2010) for four species (H, He, O, and Fe) with a range of charge-to-mass ratios. Chollet et al. (2010) considered scattering mean free paths λ ranging from 0.01 to 1 AU, and also varied the radial and rigidity dependence of λ. Surprisingly, the source energy required to account for the accelerated particles in these different scattering descriptions varied by less than a factor of ~2. This is apparently because the scattering and energy-loss processes compensate for each other—the more particles scatter the more often they cross 1 AU, but they also lose more energy in the process. In this paper, we have used their form of λ derived from quasi-linear theory (see Equation (3) in Chollet et al. 2010).

To relate the measured near-Earth values of MeV cm^{-2} to the integrated contribution of SEPs escaping through a 1 AU sphere surrounding the Sun, we need to know how SEPs from a given source location are distributed in longitude and latitude. Emslie et al. (2004) assumed that the SEP fluence at Earth falls off exponentially with e-folding separations of 35° for latitude, 45° for longitude in western events, and 25° for longitude in eastern events. Since then, Lario et al. (2006) have measured the longitudinal distribution of SEPs using two- and three-spacecraft data from the two *Helios* spacecraft and the *Interplanetary Monitoring Platform-8* (*IMP-8*). They adopted a Gaussian spatial distribution given by $F = F_o \exp[-(\Phi - \Phi_0)^2/2\sigma^2]$, where Φ is the longitude of the observer, Φ_0 is located 25°.8 east of the point of best solar wind connection for a 450 km s^{-1} solar wind (~W52°), and $\sigma = 38°$. We use their result for the fluence of 4–13 MeV protons and we assume it also applies to latitude differences. By using this relation with the measured flare location and the near-Earth value for the escaping MeV cm^{-2}, we obtained the source energy required to supply SEPs escaping over a 1 AU sphere centered on the Sun. The results are tabulated in the "SEP" column of Table 1. Note that we have limited this study to SEP events with source regions ranging from E60° to W90° in longitude. Beyond this range the Gaussian longitude distribution adopted by Lario et al. (2006) drops off very rapidly and the longitude corrections become considerably greater and more uncertain. The typical uncertainty in SEP energy is conservatively estimated to be a factor of three.

2.8. Non-potential Energy in the Active Region Magnetic Field

It is commonly believed that the fundamental energy source for an SEE lies in current-carrying magnetic fields. In such a scenario, the free energy available to power the event is the excess "non-potential" magnetic energy—the energy above the minimum-energy, potential (i.e., current-free) field to which the field can relax. The estimated available non-potential magnetic energies of the active region producing the SEEs are listed in the column labeled "Mag" of Table 1. The estimates were made from full-disk LOS magnetograms obtained from the Michelson Doppler Imager (MDI; Scherrer et al. 1995) on *SOHO*, using the method described by Welsch et al. (2009) and outlined below.

The 2002 July 20 event (Event 5) was located behind the east limb. Although its source is therefore uncertain, subsequent active region maps suggest that this event probably occurred in AR 10039, the same source region for the 2002 July 23 event (Event 6). Consequently, the estimated non-potential magnetic energy for the latter event is a plausible estimate for the non-potential magnetic energy in the former, and indeed the use of such an estimate is consistent with the procedure used to estimate the non-potential magnetic energy content in other near-limb events (e.g., W72° for 2002 February 20 (Event 1) and W84° for 2002 April 21 (Event 2)), for which magnetic field measurements obtained when the pertinent active region was near to disk center were used. However, because there is still a finite possibility of misidentification of the active region, we have chosen not to use this estimated value either in Table 1 or in the pertinent plots of Section 3.

Numerous efforts have been undertaken to estimate non-potential magnetic energies in active regions near disk center. The methods include: (1) using the magnetic virial theorem estimates from chromospheric vector magnetograms (Metcalf et al. 1995, 2005), (2) semiempirical flux-rope modeling using Hα and EUV images with MDI LOS magnetograms (Bobra et al. 2008), and (3) MHD modeling (Metcalf et al. 1995; Jiao et al. 1997) and non-potential field extrapolation based upon photospheric vector magnetograms (Guo et al. 2008; Schrijver et al. 2008; Thalmann & Wiegelmann 2008; Thalmann et al. 2008). These methods are labor intensive, and uncertainties in their energy estimates are large. For example, error bars on virial free-energy estimates can exceed the potential magnetic energy. Also, there is considerable scatter in estimates from studies that employ several methods to analyze the same data (e.g., Schrijver et al. 2008). A couple of generalizations, however, can be made. Free energies determined by virial methods matched or exceeded the potential field energy, while free energies estimated using other techniques typically amounted to a few tens of percent of the potential field energy. Published values for free energies in analytic (Schrijver et al. 2006) and semiempirical (Metcalf et al. 2008) fields meant to model solar fields also hover around a few tens of percent of the potential field energy.

We estimated the free (i.e., non-potential) magnetic energies listed in Table 1 to be 30% of the potential magnetic energy determined from MDI full-disk LOS magnetograms. This is believed to be a conservative estimate but it has the advantage that it can be readily determined for most of the events. Some of the events arose from limb active regions, for which simultaneous magnetograms are unavailable. Even if vector magnetograms were available, uncertainties in free energies would still be large. With published virial free-energy estimates ranging to a few times the potential energy, it is possible that the true free energy could exceed our estimates by a factor of ∼10.
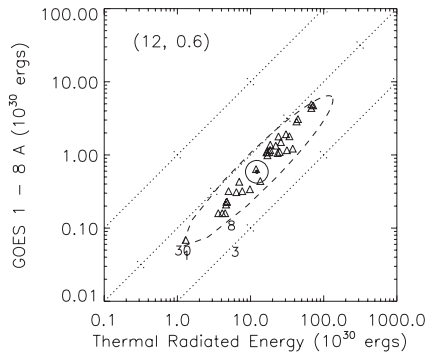
Apart from two cases where flux was clearly emerging near the time of the event (Events 29 and 38), we calculated the potential magnetic energies from magnetograms in which each event's source active region was near the disk's central meridian, assuming a rigid rotation rate of $13°$ day^{-1}. This means the energy estimates were sometimes made a few days before or after a given event. Fields were assumed to be radial, so each pixel's LOS field strength B_{LOS} was divided by the cosine of the heliocentric angle between the pixel and the sub-observation point, to generate an estimated radial field, B_R. Using a Mercator projection (Welsch et al. 2009), the corrected pixel values were then interpolated onto a two-dimensional plane. Next, the scalar potential χ, where $\mathbf{B} = -\nabla\chi$, was determined using a Green's function method. Finally, the magnetic energy U_M was estimated by integrating $(\chi B_R/8\pi)$ over manually defined cropping windows that contained each active region. Images of the magnetograms used, as well as deprojected data with cropping windows, are online at *http://solarmuri.ssl.berkeley.edu/~welsch/public/meetings/ SADOSC24/*.

In several cases in Table 1 (e.g., Events 22–25), the same value of the magnetic energy is given to adjacent events up to five days apart from the same active region. This is because the magnetic energy was estimated from LOS magnetograms taken when the active region was close to disk center. These estimates become increasingly unreliable as the active region moves away from disk center. Thus, although it is very likely that the active region's magnetic fields evolved substantially over the time between events, there is no way to reliably quantify these changes from the available magnetograms. This problem will be alleviated with the now regularly available vector magnetic field measurements from the Helioseismic and Magnetic Imager (HMI; Scherrer et al. 2012) on the *Solar Dynamics Observatory* (*SDO*), which can be used to estimate the energy in regions located away from disk center.
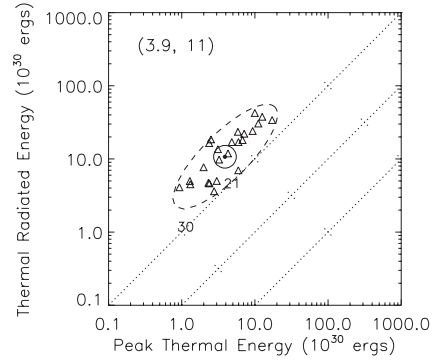
3. COMPARISONS OF ENERGETIC COMPONENTS

In this section, we present comparisons of the energy contents of the various components discussed above, through a series of figures each showing logarithmic scatter plots (the "forest") of the energy content of one component versus the energy content of another, for all events ("trees") for which data are available for both selected components. The scatter of the points around the logarithmic centroid is due both to the true range of energies of the selected events and to the often large uncertainties (up to 2.5 orders of magnitude in some cases) in the energy estimates of each component. If the uncertainties are random, then the centroid location gives an indication of the average ratio of the energies of the two components being plotted, and the scatter of the points about the centroid provides a measure of the overall uncertainty in that ratio. Any "outlier" point indicates an anomalous event, which could simply identify an unusually large or small event, or which could reveal intrinsic differences in the distribution of energies between the different components or some error in the energy estimates for the event in question.
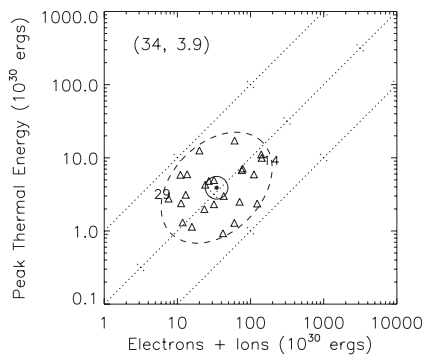
The component energy comparisons are discussed in the following subsections, with associated plots given in Figures 1–3. All plots have the same four orders-of-magnitude range on each axis, so that the degree of spread in a particular energetic component can be readily visualized. In each plot, all events that have measured energies for both components are shown. The points
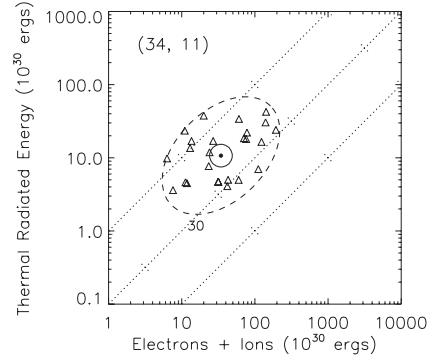
(a) GOES 1–8 Å band vs. the total energy radiated from the SXR-emitting plasma.

(b) Total energy radiated from the SXR-emitting plasma vs. the peak thermal energy content of that plasma.

(c) Peak thermal energy in the SXR-emitting plasma vs. energy in flare-accelerated nonthermal particles (electrons plus ions when available).

(d) Thermal radiated energy from the SXR-emitting plasma vs. the energy in flare-accelerated nonthermal particles (electrons plus ions when available).

Figure 1. Scatter plots of different energy components, in units of 10^{30} erg. Each plot includes all events for which measurements are available for both components. The points are indicated by triangles, except for the "outlier" points lying outside the 2σ ellipse (see below), which are instead labeled by their event numbers (Table 1) and are located at the center of the respective numbers. The location of the logarithmic centroid, defined by Equation (A1), for all the events in the plot is shown by a bull's eye with its X and Y coordinates listed in the upper left corner of the plot. The three diagonal dashed lines represent the 1%, 10%, and 100% ratios between the plotted components. Lines of constant logarithmic average event energy are shown by tick marks every order of magnitude along the lines of constant ratio. The major and minor axes of the ellipse are defined by ± 2 times the rms deviation of the points, respectively, parallel (Equation (A5)) and perpendicular (Equation (A4)) to the line of constant ratio passing through the centroid (see the text and Appendix for discussion). Points outside this ellipse are considered as outliers and are discussed in Section 5.

are indicated by triangles, except for the "outlier" points lying outside the 2σ ellipse (see below), which are instead labeled by their event numbers (Table 1) and are located at the center of the respective numbers. Events with only upper and/or lower limits are generally not shown. However, we have included pertinent data for the behind-the-limb Event 5 and for Event 25, for which there is some ambiguity in the CME kinetic energy and we have hence used the geometric mean of the two estimates. The logarithmic centroid is shown by a bull's eye with its X and Y coordinates, calculated using Equation (A1), given in the upper left corner of the plot. The three diagonal dotted lines are lines of constant ratio R as defined by Equation (A2), with $R = Y/X = 100\%$, 10%, and 1%. These lines each have tick marks showing the overall "size" of the event $A = \sqrt{XY}$—see Equation (A3). The dashed-line ellipse shows the $\pm 2\sigma$ locus; the widths of this ellipse perpendicular (Equation (A4)) and parallel (Equation (A5)) to the lines of constant ratio are measures of the 2σ spread in the energy ratio, R, and the event size, A, respectively. Points outside this ellipse are considered as "outliers" and will be discussed in Section 5.

Table 3 lists, for each plot, the energetic components involved, the value of the logarithmic centroid energies and their ratio, and the root mean square (rms) spreads in the values of the ratio R and the size A. Also, to quantify possible trends of one parameter versus the other, Table 3 lists the Spearman's rank correlation coefficient ρ, a quantity that measures the correlation between their rank orders (lowest → highest) of the variables. The formal equations used to determine these different parameters are given in the Appendix.

3.1. Radiated Energy in the GOES 1–8 Å Band versus Radiated Energy from SXR-emitting Plasma

Figure 1(a) shows the scatter plot for the radiated energy in the *GOES* 1–8 Å band versus the total energy radiated from the hot SXR-emitting plasma. The points are closely rank-correlated ($\rho = 0.96$) and also cluster very closely in the perpendicular (R) direction, showing that the energy radiated in the *GOES* 1–8 Å band is a relatively constant fraction ($R = 0.05$) of the total energy radiated from the SXR-emitting plasma. Indeed, a regression analysis of the data in Table 1 shows that the
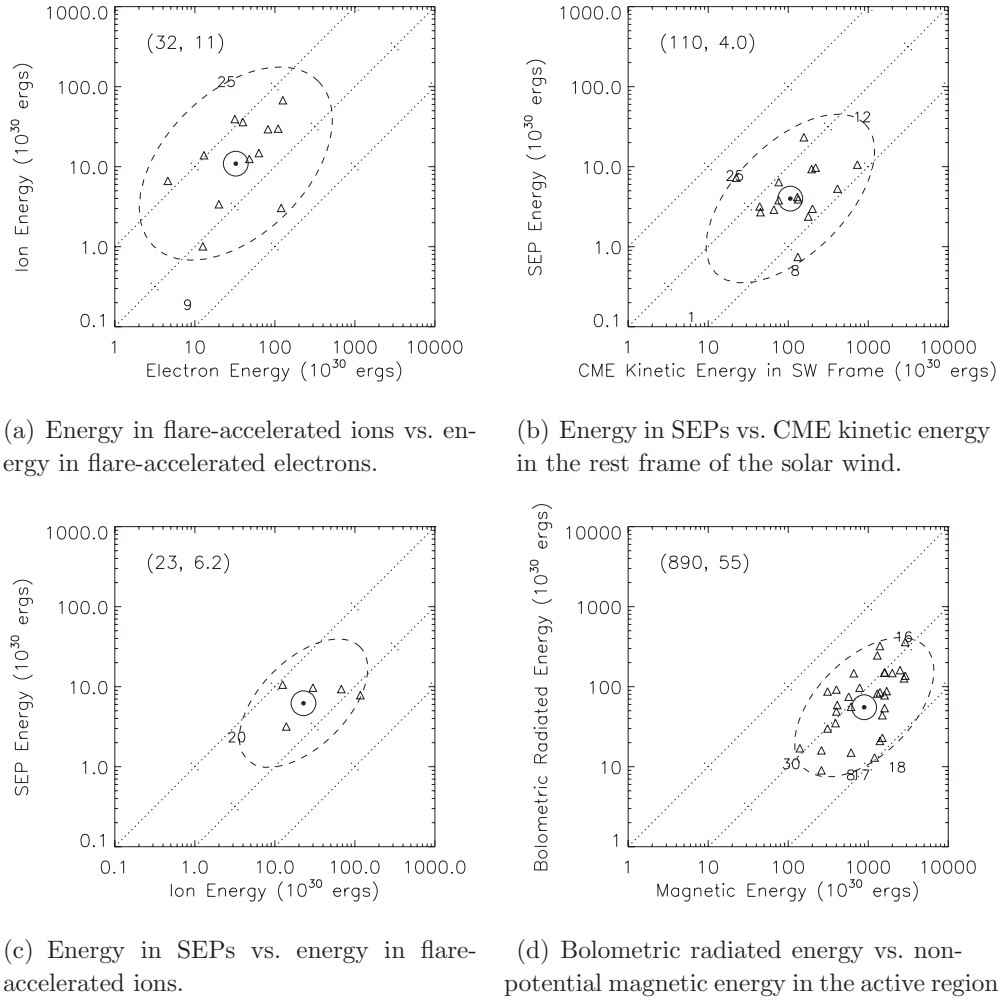
(a) Energy in flare-accelerated ions vs. energy in flare-accelerated electrons.

(b) Energy in SEPs vs. CME kinetic energy in the rest frame of the solar wind.

(c) Energy in SEPs vs. energy in flare-accelerated ions.

(d) Bolometric radiated energy vs. non-potential magnetic energy in the active region.

Figure 2. Same as Figure 1 for different combinations of energy components, as indicated on the axis labels.

Table 3
Parameters Represented in Scatter Plots

Figure No.	Plotted Components		Log. Centroid[a]		R[b]	rms[c]		ρ[d]	No. of Events
	X-Axis	Y-Axis	X (10^{30} erg)	Y (10^{30} erg)		R	A		
1(a)	Rad. from hot plasma	*GOES* 1–8 Å	12	0.6	0.05	0.17	0.51	0.96	38
1(b)	Peak thermal energy	Rad. from hot plasma	3.9	11	2.7	0.22	0.34	0.82	26
1(c)	Electrons+ions	Peak thermal energy	34	3.9	0.11	0.43	0.31	0.36	26
1(d)	Electrons+ions	Rad. from hot plasma	34	11	0.31	0.43	0.34	0.46	26
2(a)	Electrons	Ions	32	11	0.34	0.63	0.52	0.45	14
2(b)	CME KE (SW frame)	SEP	110	4.0	0.04	0.49	0.47	0.47	20
2(c)	Ions	SEP	23	6.2	0.27	0.38	0.35	0.20	6
2(d)	Magnetic	Bolometric	890	55	0.06	0.43	0.38	0.56	37
3(a)	Magnetic	CME KE+PE	1000	200	0.19	0.39	0.34	0.68	23
3(b)	CME KE+PE	Bolometric	200	71	0.35	0.43	0.38	0.54	24
3(c)	Bolometric	Electrons+ions	49	34	0.71	0.47	0.35	0.37	26
3(d)	Bolometric	Rad. from hot plasma	57	12	0.21	0.21	0.47	0.92	38

Notes.
[a] X and Y values of the logarithmic centroid, computed using Equation (A1).
[b] $R = Y/X$, the ratio of Y and X values of the logarithmic centroid computed using Equation (A2).
[c] rms (root mean square) values of $R = Y/X$ and $A = \sqrt{XY}$, computed using Equations (A4) and (A5). The rms values of R and A, respectively, quantify the scatter perpendicular and parallel to the line of constant energy ratio that passes through the logarithmic centroid.
[d] Spearman's rank correlation coefficient—a non-parametric measure of statistical dependence between two variables—see Equation (A6).
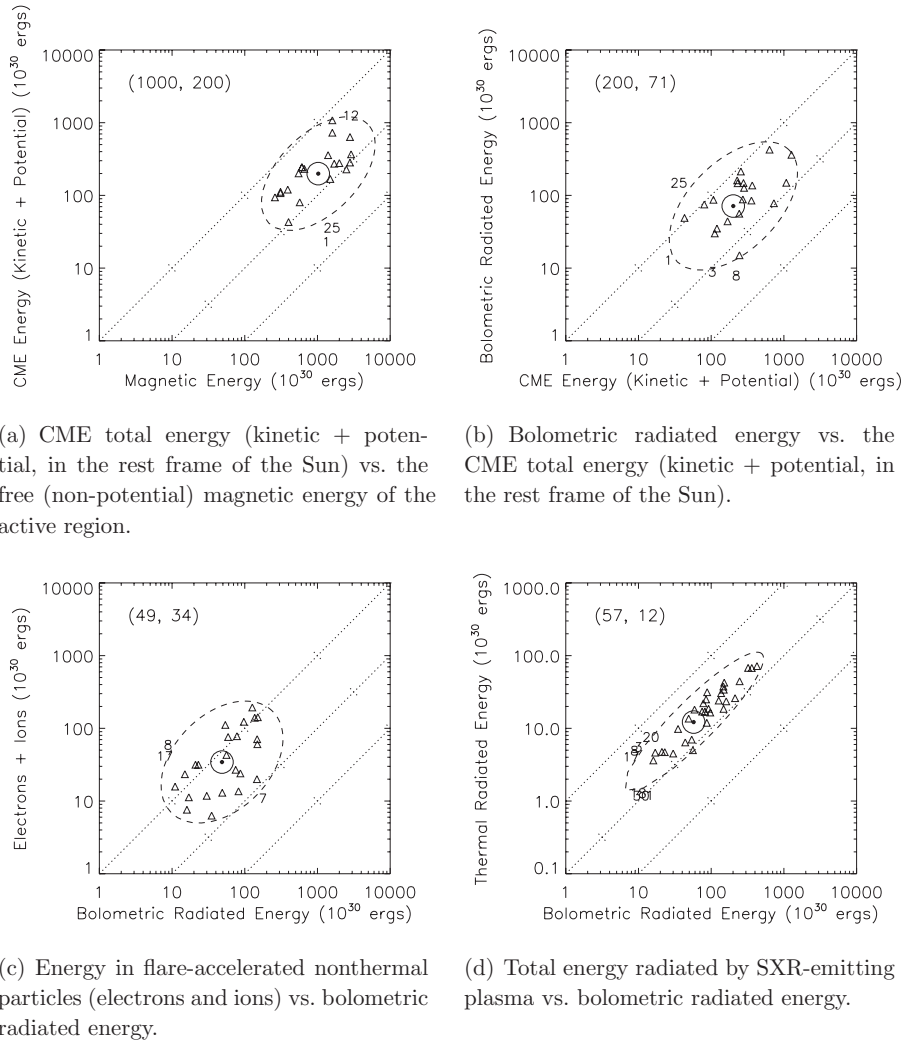
(a) CME total energy (kinetic + potential, in the rest frame of the Sun) vs. the free (non-potential) magnetic energy of the active region.

(b) Bolometric radiated energy vs. the CME total energy (kinetic + potential, in the rest frame of the Sun).

(c) Energy in flare-accelerated nonthermal particles (electrons and ions) vs. bolometric radiated energy.

(d) Total energy radiated by SXR-emitting plasma vs. bolometric radiated energy.

Figure 3. Same as Figure 1 for different combinations of energy components, as indicated on the axis labels.

ratio (best estimate $\pm 1\sigma$) of the total energy radiated by SXR-emitting thermal plasma in the flare to the observed *GOES* 1–8 Å flux is 15.4 ± 0.8. This strong correlation is not surprising since both energy components plotted are calculated from the *GOES* SXR fluxes; the scatter about the trend line arises from the differences in the temperatures of the different events.

3.2. Thermal Radiated Energy versus Peak Thermal Energy

Figure 1(b) shows the scatter plot of the total energy radiated from hot SXR-emitting plasma versus the peak thermal energy content of that plasma. The relatively tight correlation ($\rho = 0.82$) between these two components is expected, since both parameters refer to the same SXR-emitting plasma. Event 30 (the M6.4 event on 2005 August 25) is the most extreme outlier but it is almost equally weak in both energy components. On average, the total energy radiated exceeds the peak thermal energy content by a factor of ~ 3 ($R = 2.7$ in Table 3), implying continuous re-energization of the SXR-emitting material as the flare progresses.

3.3. Peak Thermal Energy versus Energy in Flare-accelerated Nonthermal Particles

Figure 1(c) shows the scatter plot for the peak thermal energy in the hot SXR-emitting plasma versus the energy in flare-accelerated nonthermal particles (electrons plus ions, when

available). There is substantially greater spread in the points compared to Figure 1(b), but nevertheless a reasonable bunching of the points. The maximum spread of the points is less than two orders of magnitude in either parameter. On average, the energy in the flare-accelerated nonthermal particles exceeds the peak thermal energy by almost an order of magnitude ($R = 0.11$), indicating that there is easily sufficient power in the particles to create the SXR-emitting thermal plasma. This conclusion is reinforced by the fact that the energy in flare-accelerated electrons is a lower limit (see Section 2.4) and is in agreement with earlier comparisons of flare-accelerated electrons versus peak thermal energy—see, e.g., de Jager et al. (1986) and Saint-Hilaire & Benz (2002).

3.4. Thermal Radiated Energy versus Energy in Flare-accelerated Nonthermal Particles

Figure 1(d) shows the scatter plot for the total energy radiated by the SXR-emitting thermal plasma versus the energy in flare-accelerated nonthermal particles (electrons and ions when available). This figure combines information already evident in Figures 1(b) and (c). It shows that the energy in accelerated electrons and ions during a flare is not only sufficient to supply the peak energy of the SXR-emitting plasma (Figure 1(c)), but it is also high enough (by a factor of ~ 3, $R = 0.31$) to account for the radiation from this plasma throughout the

event. As discussed in Section 2, it follows that a significant fraction of the energy in flare-accelerated nonthermal particles is deposited by thermal conduction into lower-temperature plasma and ultimately radiated in optical and EUV wavebands (see Emslie et al. 2005). Again, Event 30 (the M6.4 event on 2005 August 25) is the only "outlier" in this plot, reflecting the low values of both the thermal and nonthermal energy components.

3.5. Flare-accelerated Ions versus Electrons

Figure 2(a) shows the scatter plot for the energy in flare-accelerated ions, as determined from the *RHESSI* gamma-ray observations (Section 2.5), versus the energy in flare-accelerated electrons, as determined from *RHESSI* hard X-ray observations (Section 2.4).

As pointed out in Section 2.4, the energy in electrons is critically dependent on the low-energy cutoff, E_{min}, that is assumed for the electron spectrum. Since the largest value of E_{min} that gives an acceptable fit to the data is used for each spectrum, the total electron energy values are lower limits with order-of-magnitude uncertainties. As explained in Section 2.5, the situation for the ion energies is even worse, both because of the spread in the observed 2.223 MeV fluences and because of the need to extrapolate the ion flux at energies above 30 MeV, as derived from these 2.223 MeV line fluences, to the ion flux above 1 MeV. Because of these large uncertainties in both the electron and ion energies, there is a much wider scatter than in the plots in Figure 1. However, with some notable exceptions that have almost two orders of magnitude more energy in the electrons than in the ions (Events 9 and 15), the electron and ion energies are generally comparable within an order of magnitude. This result is in agreement with the claims by Ramaty et al. (1995) and Ramaty & Mandzhavidze (2000) and has significant consequences for particle acceleration models.

3.6. SEP Energy versus CME Kinetic Energy in the Solar Wind Rest Frame

Figure 2(b) shows the scatter plot for the energy in the accelerated SEP population versus the kinetic energy of the CME in the rest frame of the solar wind. We use the solar wind rest frame since a shock can be formed and SEPs accelerated only if the CME is traveling at least as fast as the solar wind speed (Mewaldt et al. 2008a). Lacking knowledge of the solar wind speed low in the corona for each event, we have simply subtracted 400 km s^{-1} from the measured CME speed in order to estimate the kinetic energy available for accelerating particles via shock acceleration.

Most of the SEP values cluster between 1% and 10% of the CME kinetic energy. Comparing the nine events that are common to both Mewaldt et al. (2008b) and this study (Events 2, 4, 7, 8, 11, 12, 13, 14, and 16), the SEP/CME ratio was 5.8% in Mewaldt et al. (2008b) and is 4% here ($R = 0.04$ in Table 3). Overall, as a result of several changes in the analysis, the SEP energy estimates in this paper are reduced from those in Mewaldt et al. (2005, 2008b) by an average of 40%. One of these changes is the adoption of the longitude correction of Lario et al. (2006), which results in changes of as much as a factor of two in the energy estimates of individual SEP events. For the nine events in common with this paper and Mewaldt et al. (2008b), the differences due to longitude/latitude corrections alone ranged from −52% to +51% with a mean difference of −16%; for all 20 events shown in Figure 2(b), the average effect is a ∼10% decrease in energy. Another change is the adoption

of new corrections for particles crossing 1 AU multiple times and for adiabatic energy loss that are based on the energy- and species-dependent simulations of Chollet et al. (2010); these changes resulted in a further decrease averaging ∼30% in the SEP energy content of the nine events in common with Mewaldt et al. (2008b). Finally, the SEP spectra in this study were integrated from 0.03 MeV nucleon^{-1} to 300 MeV nucleon^{-1}, rather than from 0.01 MeV nucleon^{-1} to 1000 MeV nucleon^{-1} as in Emslie et al. (2004) and Mewaldt et al. (2005, 2008b). The increase in the low-energy limit to 0.03 MeV nucleon^{-1} represents a more realistic threshold for injection into the shock acceleration process (see, e.g., Li et al. 2012), and results in a typical reduction in the energy content by ∼5%. The change in the upper limit has a negligible effect.

Overall, this new analysis confirms that the SEP energy is a small, but not insignificant, fraction of the CME kinetic energy in most large events.

3.7. SEP Energy versus Energy in Flare-accelerated Ions

Figure 2(c) shows the scatter plot for the total energy in SEPs versus the energy in flare-accelerated ions, as determined from *RHESSI* gamma-ray observations. There are only a limited number of events that can be compared, but in those few cases there is comparable energy in the ions and SEPs ($R = 0.27$). At first sight, this appears to conflict with the study by R. A. Mewaldt (2012, in preparation) that shows the number of >30 MeV SEP protons measured in interplanetary space is generally much higher than the number of >30 MeV protons interacting in the solar atmosphere (Shih et al. 2009). However, this difference can be accounted for in a number of ways. First, as noted in Section 2.5, the inferred energy in flare-accelerated ions is based on a very uncertain spectral extrapolation over more than an order of magnitude in proton energy (from 30 MeV down to 1 MeV). To obtain the energy in flare-accelerated ions (Section 2.5), we have assumed a spectral index of 4, which results in a significantly higher total energy than would be obtained if the extrapolation was performed with the much lower spectral indices representative of SEP spectra measured in situ at 1 AU. Further, for the well-observed 2003 October 28 flare (Event 12), we obtained an ion spectral index of 3.4 at energies between ∼3 and 50 MeV, so that the energy content in ions could be significantly lower than we have used here, especially if the spectrum hardens even more between, say, 1 and 20 MeV, a feature that is clearly seen in SEP spectra. Second, SEP protons typically carry ≳80% of the SEP ion energy, whereas flare-accelerated protons carry only about one-third of the ion energy.

3.8. Bolometric Radiated Energy versus Magnetic Energy

Figure 2(d) shows the scatter plot for the bolometric radiated energy versus the non-potential (free) magnetic energy in the active region. Here, we have a relatively tight bunching with little more than 1.5 orders of magnitude range in each parameter. It should be emphasized that the plotted bolometric radiated energies are, with the exception of the five events noted in Table 1, not directly measured but rather estimates made using the FISM model (Chamberlin et al. 2007, 2008), and the magnetic energy is only good to an order of magnitude. With this proviso, we find that the average bolometric radiated energy is ∼6% of the free magnetic energy ($R = 0.06$), and in all cases the available magnetic energy exceeds the bolometric radiated energy by at least half an order of magnitude. This is consistent with the well-accepted notion that the reservoir of magnetic energy is sufficient to power the main components of the flare.

3.9. CME Energy versus Magnetic Energy

Figure 3(a) shows the scatter plot for the CME total energy (potential + kinetic) in the rest frame of the Sun versus the non-potential energy in the magnetic field. The CME energy is, on average, only a small fraction ($R = 0.19$) of the magnetic energy, similar to the value $R = 0.06$ found for the ratio of bolometric radiated energy to magnetic energy (Section 3.8; Figure 2(d)). While bearing in mind the very approximate values of the latter, it nevertheless appears, from the results of this and the previous subsection, that much of the available magnetic energy (some two-thirds) is retained in the active region (i.e., the field does not return to a fully potential state), even after the flare and the ejection of the CME. This result is consistent with the generous limits established by Moore et al. (2012) on the possible free energy that an active region magnetic field can hold before it erupts.

3.10. Bolometric Radiated Energy versus CME Energy

Figures 2(d) and 3(a) show, respectively, that the available magnetic energy is about 15 times the bolometrically radiated energy in the flare ($R = 0.06$) and about 5 times the CME energy ($R = 0.19$). Given the substantial overlap of events common to both plots (Tables 1 and 3), this indicates that, on average, the energy in the CME is larger than the energy radiated by a factor of ~3. Figure 3(b) confirms this result by showing the scatter plot for bolometric radiated energy versus the CME total energy (kinetic + potential). On average, the bolometric energy is indeed about half an order of magnitude less than the CME energy ($R = 0.35$).

3.11. Flare-accelerated Particle Energy versus Bolometric Radiated Energy

Figure 3(c) shows the scatter plot for the total energy in flare-accelerated particles (electrons plus ions) versus the bolometric radiated energy. This figure shows that the energy in accelerated particles during a flare is comparable to the total bolometric radiated energy from the flare ($R = 0.71$), with the ratio being greater than unity in some events and less than unity in others. It must be recalled that while the bolometric radiated energies are accurate to within a factor of ~2 to 3, the energies in flare-accelerated particles are uncertain to at least an order of magnitude. The energies in electrons are most probably lower limits and may well underestimate the true energy content by up to an order of magnitude. The energies in ions may, however, be overestimates, depending on the power-law index used for the spectral extrapolation. We can tentatively conclude, however, that there is sufficient energy in the flare-accelerated particles to account for *all* the energy radiated in the flare. However, this conclusion must somehow be verified by more accurate estimates of the energy in the flare-accelerated electrons and ions.

3.12. Energy Radiated by Soft X-Ray Emitting Plasma versus Bolometric Energy

Figure 3(d) shows the scatter plot for the total energy radiated by SXR-emitting plasma versus the bolometric radiated energy. The relatively tight correlation ($\rho = 0.92$) is to a large extent due to the fact that most of the bolometric radiant energies were computed using the FISM model, which uses the radiated energy from SXR-emitting plasma to estimate the bolometric energy. Nevertheless, the data show that only about one-fifth of the bolometric energy radiated by a flare is radiated by the SXR-emitting plasma ($R = 0.21$).

4. DISCUSSION

The comparisons of the energetics of the different components shown in the scatter plots of Figures 1–3 are summarized in Table 3.

In attempting to draw any definitive conclusions from these comparisons, we must keep in mind the limitations of our analysis. The events in our list cover the period from *RHESSI*'s launch in February 2002 through 2006. They include 9 of the 11 X5 or greater events that occurred in this time period. They also include the largest SEP events and all significant *RHESSI* gamma-ray line events, and hence represent events where a significant number of ions were accelerated to high energies, either in the flare, at the CME shock, or at both locations. Most of the CMEs that we have included have kinetic energies of $\gtrsim 10^{32}$ erg. According to Figure 8 of Gopalswamy et al. (2004), only 16 CMEs observed from 1997 to 2002 had kinetic energy $> 1.4 \times 10^{32}$ erg. Adding in the five CMEs with kinetic energy $> 1.4 \times 10^{32}$ erg that occurred in 2003 (Events 11, 12, 13, 14, and 16 in Table 1), we see that only 21 CMEs with kinetic energy $\gtrsim 10^{32}$ erg occurred during 1997–2003. For this period, Gopalswamy (2006) reports a total of 4133 CMEs, with average kinetic energy 5×10^{29} erg. Therefore, if we consider the 1997–2003 period as typical, only $21/4133 \simeq 0.5\%$ of all CMEs have kinetic energies as large as those considered in this paper. In summary, the events studied represent the largest SEEs that occurred during the period in question.

Despite the relatively large number of events in our list, the range of energies is typically only about two orders of magnitude in any of the energy components. The uncertainties on the energy estimates of each component are generally at least an order of magnitude, except for the few cases where the bolometric radiated energy is measured with an accuracy of a factor of ~2. Thus, in most cases, we cannot expect to see any significant trends with the size of the events over the limited range of our selected events. In spite of these selection effects and measurement limitations, the scatter plots nevertheless reveal several useful results regarding large SEEs in general and about specific events in particular. With a few notable exceptions, the points in each plot are bunched together within the expected order-of-magnitude uncertainties. However, there is substantially more scatter of the points in some parameters than others. Only a few events stand out as outliers in certain plots; these outliers are discussed in Section 5.

The general bunching of the data points in each scatter plot is characterized by the logarithmic rms deviations parallel and perpendicular to the line of constant ratio that passes through the logarithmic centroid. The *X* and *Y* values of the centroids are shown on each plot and listed along with the rms values in Table 3. The fact that the data points generally bunch together can be interpreted as an extension to SEEs of the "*big flare syndrome*" (BFS), a phrase coined by Kahler (1982) based on the strong correlations between proton fluxes and associated microwave and hard X-ray burst parameters, and a concept which has since come to mean that each flare component scales roughly linearly with some absolute measure of flare "size." At that time, before the so-called *solar flare myth* was exposed (Gosling 1993), it was not clear that SEPs were generally more likely to be accelerated at CME shock fronts, but now the same concept can be applied to include CMEs with flares and SEPs. From our data, it is clear that, with some caveats, the BFS concept can be applied to all energetic SEE phenomena, including the CME energy.

Notable exceptions to the scatter of the points being consistent with the expected uncertainties in each parameter are the following.

1. The plot of the *GOES* 1–8 Å integrated energy versus the total energy radiated from the SXR-emitting plasma over all wavelengths (Figure 1(a)) shows that these two parameters are well correlated (the Spearman's rank correlation coefficient ρ given in Table 3 is 0.96, the highest for any pair of parameters). This is not surprising since the measurements of the two parameters are not independent—they both use the same *GOES* X-ray data. The scatter of the points thus reflects only the range of flare sizes and the different temperatures—the scatter perpendicular to the line of constant ratio, only about half an order of magnitude, is the result of different temperatures, while the scatter parallel to that line is almost two orders of magnitude, reflecting the range of flare intensities. A regression analysis of the data in Table 1 shows that the ratio (best estimate ± standard error) of the total energy radiated by SXR-emitting thermal plasma in the flare to the observed *GOES* 1–8 Å flux is 15.4 ± 0.8, i.e., that the energy radiated in the *GOES* 1–8 Å band is about one-fifteenth to one-twentieth ($R = 0.05$) of the total energy radiated by the SXR-emitting plasma over all wavelengths. The presence of the outlier points for Events 3 and 8, several rms values away from the line of constant ratio, suggests that these two events are different in that their temperature is lower than the average. This is consistent with the conclusion reached by Feldman et al. (1996) and Garcia (2004) that lower temperatures are generally associated with smaller X-ray peaks.

2. The range of the ion energies—about three orders of magnitude—is larger than for all other parameters. This range is especially evident in Figure 2(a), which shows the scatter plot for the energy in flare-accelerated ions as determined from the *RHESSI* gamma-ray observations (Section 2.5) versus the energy in flare-accelerated electrons as determined from *RHESSI* hard X-ray observations (Section 2.4). Since the ion energy content above 1 MeV was deduced by applying the same $\delta = 4$ spectral extrapolation to the energy content above 30 MeV in all events, this large range in energy contents above 1 MeV mirrors exactly the spread in the energy contents above 30 MeV and hence the spread in the observed 2.223 MeV line fluences. However, it must be noted that uncertainty in the value of δ results in a further large uncertainty in the ion energy content above 1 MeV for any specific event, since this quantity is derived through spectral extrapolation over one-and-a-half orders of magnitude in ion energy (Section 2.5). This uncertainty would act to *increase* the scatter in the energy content above 1 MeV if the value of δ was positively correlated with the value of the >30 MeV energy content; alternatively, it would act to *decrease* the scatter in energy content >1 MeV if the value of δ was negatively correlated with the value of the >30 MeV energy content. In this context, it should be noted that Shih et al. (2009) found a strong correlation, over more than three orders of magnitude, between the energy in flare-accelerated ions and the energy in electrons above 300 keV (rather than the ∼20 keV lower cutoff energy used here). This suggests that steep (shallow) spectra (high (low) values of δ) are associated with low (high) values of the energy content at high energies, and therefore that

use of individual spectral indices to create more accurate energy estimates of the ion energy content above 1 MeV might reduce the scatter in the plot.

5. DISCUSSION OF OUTLIER DATA POINTS

While most of the events in Table 1 lie (by definition) within the 2σ ellipses in the various cross-correlation plots, there are a few notable exceptions. We now discuss these "outliers" and the possible reasons for their unusual energetic partitioning.

1. *Event 1*. This M5.1 event, on 2002 February 20, is one of the two events with a relatively low ratio of CME energy (kinetic + potential) to magnetic energy (Figure 3(a)). Table 1 shows a paucity of data for other energetic components. Data for *GOES* 1–8 Å emission and total radiated energy from the SXR-emitting plasma are available; the event does fall outside the 2σ ellipse in Figure 1(a), but only by virtue of its overall weakness, not the ratio of *GOES* 1–8 Å emission to total SXR-emitting energy. We believe that this is therefore simply a weak event, in which only a small fraction of the available magnetic energy was dissipated.

2. *Event 3*. This C5.0 event, on 2002 May 22, has a relatively low ($\lesssim 1\%$) ratio of *GOES* 1–8 Å emission to total SXR-emitting energy (Figure 1(a)). An event with limited overall information (Table 1), it does, however, appear in Figure 2(b), where a normal ratio of SEP to CME energy is evident. It should be noted that this is the only *GOES* C-class event in Table 1 and we therefore simply categorize this event as a weak *GOES* event, possibly due to the low temperature (<9 MK) of the SXR-emitting plasma. This event is the third in a sequence of events starting with an M1.5 event peaking at 21:29 UT on May 21, followed by a C9.7 event at 00:30 on May 22, and the C5.0 event in question at 03:34 UT. *RHESSI* saw parts of each of these events and the 6–12 keV images show that they came from three distinctly different locations with the following spatial centroid coordinates (in arcseconds): (−550, 270), (880, −330), and (750, −350), respectively. The peak temperatures derived from the *GOES* data for the three events are 13, 11, and 8 MK, respectively. Thus, this event was much cooler than the other larger events in our list.

3. *Event 8*. Data for this M4.6 event, on 2002 November 9, are available for all energetic components other than flare-accelerated ions (Table 1); consequently, the event appears in most of the scatter plots in Figures 1–3. In most of the plots, the event is situated within the general bunching of points. However, Figure 3(b) reveals a low ratio of bolometric energy to CME energy, while Figure 3(c) shows a similarly high ratio of energy in accelerated particles to bolometric radiated energy. Together, these point simply to an event with a relatively low bolometric radiance, as inferred from the FISM model (Section 2.2). This arises because of the relatively short duration of the *GOES* event (13 minutes from peak 1–8 Å flux to 50% of peak). As pointed out by Chamberlin et al. (2012), "the total radiated output of flares depends more on the flare duration than the typical *GOES* X-ray peak magnitude classification." The relatively low temperature of this flare (peak value of 13 MK) also explains the relatively low ratio of *GOES* 1–8 Å integrated flux to thermal radiated energy (Figure 1(a)). This event also appears in Figure 2(b) as having a marginally low ratio of SEP energy to

CME kinetic energy, but this is a presumably unrelated phenomenon.

4. *Event 9.* This X1.4 event, on 2003 May 27, has the lowest ratio of flare-accelerated ion energy to flare-accelerated electron energy (Figure 2(a)). The ratios of peak thermal energy and broadband SXR radiated energy to energy in flare-accelerated nonthermal particles are average (Figures 1(c) and (d)), and the ratio of *GOES* 1–8 Å to total SXR-emitting energy is nominal (Figure 1(a)). Shih et al. (2009) show that this flare has a ratio of accelerated $\gtrsim 20$ MeV nucleon^{-1} ions to accelerated relativistic electrons that is comparable to other gamma-ray flares, suggesting that this flare is an outlier because it has a relative deficiency in higher-energy particles, both ions and electrons. In particular, the stated ion energy content may be a significant underestimate if the ion spectrum is steeper than the $\delta = 4$ power law assumed in the extrapolation from the >30 MeV proton energy value that is obtained from the observed neutron-capture line fluence.

5. *Event 12.* This X17 event, on 2003 October 28, has relatively high CME and magnetic energies (Figure 3(a); Table 1). It was one of three events from the "Halloween" active region of 2003 October–November, in which a very high non-potential magnetic energy value (4×10^{33} erg; see Figure 2(d)) was inferred. This event is therefore an "outlier" simply because it was a very large event; there are no particularly unusual ratios of energetic components.

6. *Event 17.* The data set for this X1.6 event, on 2004 July 15, is quite extensive, with all components measured except CME and SEP energies (which are understandably absent given the $\sim$E45° location of the flare). The event has a slightly low ratio of bolometric radiant energy to magnetic energy (Figure 2(d)), and slightly high ratios of flare-accelerated particle energy to bolometric radiated energy (Figure 3(c)) and energy radiated by SXR-emitting plasma to bolometric radiated energy (Figure 3(d)). It has the equal-lowest bolometrically radiated energy content, and *the* lowest thermal energy content of SXR-emitting plasma, of any event studied (Table 1), but interestingly does *not* show as an outlier in any other plots in which it appears, notably the plot of thermal energy content versus thermal radiated energy (Figure 1(b)) and the plot of thermal energy content versus accelerated particle energy (Figure 1(c)) (although it is barely inside the 2σ ellipse in both of these plots). As with Event 8, these event properties may be explained by the relatively short SXR duration of this flare—only 4 minutes from the *GOES* 1–8 Å peak to 50% of peak flux. Although the peak plasma temperature derived from the *GOES* fluxes was 22 MK, the temperature stayed above 15 MK for only about 8 minutes. The short duration and low temperatures lead the FISM modeling process (Section 2.2) to assign a correspondingly low estimate of the bolometric radiant energy (Chamberlin et al. 2012).

7. *Event 18.* Data for this M7.1 event, on 2004 July 25, is rather limited (Table 1). The event appears as an outlier in Figure 2(d), due to a low ratio of bolometric energy to magnetic energy. Table 1 shows that this event had one of the highest inferred non-potential magnetic energy contents of all the events studied, while Figure 1(a) shows very small values of both radiation in the *GOES* 1–8 Å waveband and total energy radiated by the SXR-emitting plasma (although the ratio of the two is nominal). *RHESSI* did show a flare flag starting at 05:37 UT, but entered night at 05:42 UT, three minutes after the *GOES* start time; therefore no reliable electron or ion energy measurements are available. Further, no CME was observed for this event, which was located at approximately W30° longitude. As a result, it is not known whether the event was simply very weak radiatively, or whether only a relatively small part of the non-potential magnetic energy available was released.

8. *Event 25.* For this X7.1 event, on 2005 January 20, the ratios of nonthermal particle energy to bolometric radiated energy (Figure 3(c)), SXR-radiated to peak thermal energy (Figure 1(b)), and SXR-radiated to nonthermal particles (Figure 1(d)) are nominal. However, the ion-to-electron energy ratio ($\sim$5:1; Figure 2(a); Table 1) is conspicuously high; indeed, this event had one of the highest ion energy contents measured. This high ion-to-electron energy ratio may in part be due to the presence of high-energy protons (inferred from the 2.223 MeV line) for several minutes after most of the electron–ion bremsstrahlung had dissipated. The event also has a very low ratio of CME energy to magnetic energy (Figure 3(a)), but a very high ratio of SEP energy to CME energy (Figure 2(b)). The ratio of bolometric radiated energy to free magnetic energy is nominal (Figure 2(d)), but it is the only event with a ratio of bolometric radiated energy to CME energy that is greater than 100% (Figure 3(b)). Together, these results show that the main component that makes this event an "outlier" is the low CME energy. Note, however, that the CME kinetic energy in this event is very uncertain.

The reasons for these unusual circumstances are not completely understood. Much has been written about this event (e.g., Grechnev et al. 2008, and references therein) but the acceleration of the intense flux of SEPs has still not been fully resolved. It has been suggested that in this event the SEPs were accelerated at the flare site rather than in the CME shock (Lin 2005a, 2005b). In similar vein, Simnett (2006, 2007) concluded that, "the relativistic protons were not accelerated by the CME-driven shock." The event produced a cosmic-ray ground-level enhancement that is among the largest recorded in the history of cosmic-ray measurements (Mishev et al. 2011). However, based on the particle spectrum measured over a wide rigidity range (1–20 GV), Morgan & Lopate (2008) state that, "The 2005 January 20 GLE was an unusual event in its intensity and brevity, placing it on the outer edges of parameter space for shock acceleration to GeV energies, but still not requiring a different process, i.e., direct solar-flare acceleration." Similarly, Reames (2009) finds that SEPs in this event, as in other ground-level events (GLEs), are produced after the shock onset and do not require a separate non-shock injection. On the other hand, Moraal & McCracken (2012) conclude that neutron monitor observations of this event indicate two separate pulses of high-energy particles, one accelerated by the flare and a second accelerated by the CME-driven shock.

9. *Event 30.* This M6.4 event, on 2005 August 25, had a very low peak thermal energy content and a relatively low ratio of the total SXR-emitted energy to the peak thermal energy content (Figure 1(b)). It also has a low ratio of total SXR-emitted energy to nonthermal particle energy (Figure 1(d)). No CME or SEP data are available for this east-limb event. For this event, the *GOES* flux decayed from the M6.4 peak to the C6 level (10% of the peak flux) in only $\sim$14 minutes, so that the low values of the radiated energy in
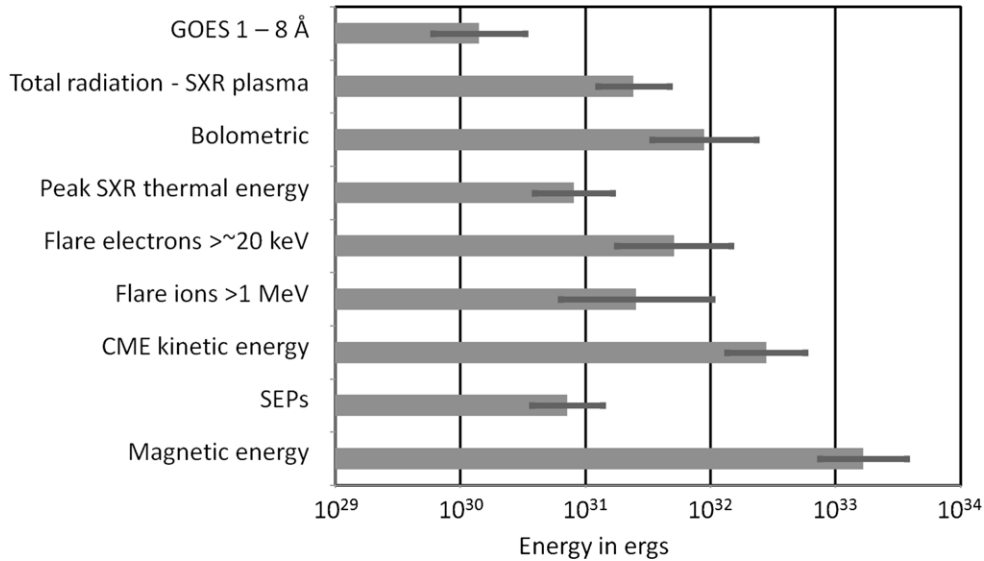
Figure 4. Bar chart showing the (logarithmic) average energies of the different components for the six events for which values were obtained for all components—Events 13, 14, 20, 23, 25, and 38. The short thin bars show the $\pm 1\sigma$ logarithmic scatter of the energies of the six events.

SXR-emitting plasma are due to this simply being a relatively short-lived event.

6. CONCLUSIONS

Despite the rather large uncertainties in the individual measurements used in this analysis, the relatively large number (38) of events nevertheless allows us to reach some general conclusions about the "typical" ratios of various energetic components in large SEEs. We have found the following general statements to hold.

1. Figure 1(b) shows that the total energy radiated by the SXR-emitting plasma over the course of the event exceeds, by about half an order of magnitude ($R = 2.8$ in Table 3), the peak energy content of the thermal plasma that produces this radiation. This reinforces the conclusions of Moore et al. (1980) that some form of energy is continuously supplied to this hot plasma throughout the event.

2. Figures 1(d) and 3(c) show that the energy content in flare-accelerated particles (electrons and ions) is sufficient to create not only the total energy radiated by the SXR-emitting plasma, but also the total bolometric radiated energy of the event.

3. Figure 2(a) shows that the energy contents of flare-accelerated ions and electrons are comparable at the order-of-magnitude level. This result supports the earlier claims of Ramaty et al. (1995) and Ramaty & Mandzhavidze (2000) and has significant consequences for acceleration models.

4. Figure 2(b) shows that the SEP energy is typically a few percent ($R = 0.04$ in Table 3) of the CME kinetic energy in the solar wind rest frame, a result with implications for shock-acceleration models of interplanetary particles.

5. The combination of Figures 2(d), 3(a), and 3(c) shows that the available magnetic energy is indeed sufficient to power the thermal plasma, flare-accelerated particles, and the CME. Although some "double-counting" may be involved in summing these energy components (e.g., both the flare-accelerated particles and the CME may transfer energy to the ambient plasma; see Emslie et al. 2005), this result nevertheless conforms to the widely held view that

the source of the energy released in SEEs lies in stressed magnetic fields.

Figure 4 shows the logarithmic average (i.e., the geometric mean) of the energies with $\pm 1\sigma$ logarithmic scatter of the various energy components for the six events (Events 13, 14, 20, 23, 25, and 38) for which *all* energetic components were measured. (Events 6 and 12 were not included, since for these events some of the components were determined only as upper or lower limits—see Table 1.) This figure, coupled with the overall ratios summarized in Table 3, succinctly demonstrates how, in very approximate terms, the available magnetic energy gets distributed in a "typical" flare in our sample:

1. Of the $\sim 10^{33}$ erg of available non-potential magnetic energy, approximately 30% is released in the SEE, with the remainder staying in the active region as stored magnetic energy. Of the $\sim 30\%$ that is released, some 80% ($\sim 25\%$ of the available energy) is released in the CME (mostly as kinetic energy) and approximately 20% ($\sim 5\%$ of the available energy) is released as flare-accelerated particles, roughly evenly distributed between electrons and ions.

2. All of the energy in the flare-accelerated particles appears to ultimately emerge as radiation across a wide range of wavelengths, from optical to SXRs (Emslie et al. 2005). However, only about one-third of the energy in flare-accelerated particles ($\sim 2\%$ of the available stored energy) is ultimately radiated from high-temperature SXR-emitting plasma. The maximum amount of energy stored as enhanced thermal energy in the SXR-emitting plasma is $\sim 1\%$ of that released, and the amount of energy radiated in the diagnostic *GOES* 1–8 Å waveband is only about 5% of the total energy radiated by the SXR-emitting plasma, or $\sim 0.1\%$ of the available magnetic energy.

3. Because of the need for a CME to "overtake" the solar wind and form a shock front where SEPs can be accelerated, only about two-thirds of the kinetic energy carried by the CME ($\sim 15\%$ of the available non-potential magnetic energy) is available for SEP acceleration. The SEP production process is in turn $\sim 4\%$ efficient, so that only about half a percent of the released magnetic energy ultimately appears in the form of SEPs.

Although for completeness we have listed Spearman's rank correlation coefficient (ρ) values in Table 3, little significance can be attached to these values other than for the obviously tight correlations between parameters that are essentially derived from the same data (e.g., the bolometric emission, the energy radiated from the SXR-emitting plasma, and the energy radiated in the *GOES* 1–8 Å band, all of which are dependent on *GOES* SXR flux measurements). Any correlations among independent components are masked by the large uncertainties in the individual measurements used in the various scatter plots. Progress in this direction will require sampling of events over a much larger range in flare size to determine if the distribution of energies among the different components found here for large events is preserved for smaller events, as would be expected for a "*big SEE syndrome*." Such a project is the next step toward a more comprehensive understanding of energy release in SEEs.

Using data from the new, more sophisticated, instruments that are now available will allow more accurate energy estimates to be made of some of the components. For example, the detailed differential emission measure analysis now possible using data from the EUV Imaging Spectrometer (Culhane et al. 2007) on *Hinode*, and from the Atmospheric Imaging Assembly (Lemen et al. 2012) and the Extreme Ultraviolet Variability Experiment (Woods et al. 2012) on the *SDO*, should lead to better estimates of the energies in the thermal plasma. Vector magnetograms from the HMI (Scherrer et al. 2012) on *SDO* allow for more accurate estimates of the energy in the non-potential magnetic field.

Other energy components not considered in our analysis may be found to contain significant total energy and should be included in any future compilation of global energetics. These include the turbulent mass motions revealed by the broadening of atomic lines seen with EUV and X-ray spectrometers (e.g., Phillips et al. 2008), and the cumulative heating of CME plasma reported by Murphy et al. (2011) to be comparable to (or even greater than) the CME kinetic energy. Another aspect not discussed here is the question of a second flare phase that, according to Woods et al. (2011) and Su et al. (2012), can release a similar amount of energy as in the initial phase. Nevertheless, we believe that the order-of-magnitude comparisons of energetic components presented herein represent a significant advance in our understanding of the nature of energy release in SEEs.

APPENDIX

Here, for definiteness, we provide the equations used to determine the values listed in Table 3: the (logarithmic) centroid energies X_{centroid} and Y_{centroid}, their ratio R, the rms (1σ) values

both perpendicular and parallel to the lines of constant ratio, and the Spearman's rank correlation coefficient ρ.

The coordinates of the logarithmic centroid in each plot are given by

$$\log_{10} X_{\text{centroid}} = \frac{1}{N} \sum_{i=1}^{N} \log_{10} X_i,$$

$$\log_{10} Y_{\text{centroid}} = \frac{1}{N} \sum_{i=1}^{N} \log_{10} Y_i, \tag{A1}$$

where N is the number of events for which there are viable measures of both components included in the scatter plot in question.

The lines of constant ratios ($R = 100\%$, 10%, and 1%) between the X and Y components satisfy the following relation:

$$R = Y/X$$
$$or \; \log_{10} R = \log_{10}(Y/X)$$
$$= \log_{10} Y - \log_{10} X. \tag{A2}$$

Lines of constant logarithmic average event energy ($\log_{10} A$), shown in the plots as tick marks every order of magnitude along the lines of constant ratio, are defined as follows:

$$\log_{10} A = (\log_{10} X + \log_{10} Y)/2$$
$$= \log_{10} \sqrt{XY}. \tag{A3}$$

The rms deviations of the points perpendicular to and parallel to the line of constant ratio passing through the centroid are defined by

$$\text{rms}_\perp = (1/N) \sqrt{\sum_i (\log_{10} R_i - \log_{10} R_{\text{centroid}})^2}$$
$$= (1/N) \sqrt{\sum_i (\log_{10}(Y_i/X_i) - \log_{10}(Y_{\text{centroid}}/X_{\text{centroid}}))^2} \tag{A4}$$

and

$$\text{rms}_\parallel = (1/N) \sqrt{\sum_i (\log_{10} A_i - \log_{10} A_{\text{centroid}})^2}$$
$$= (1/2N) \sqrt{\sum_i [\log_{10}(X_i Y_i) - \log_{10}(X_{\text{centroid}} Y_{\text{centroid}})]^2}. \tag{A5}$$

These rms values were used to draw the ellipse with axes of $2 \times \text{rms}_\perp$ and $2 \times \text{rms}_\parallel$ around the logarithmic centroids in each plot.

The Spearman's rank correlation coefficient ρ is calculated by first assigning ranks $x_i (= 1, \ldots, N)$ and $y_i (= 1, \ldots, N)$ to the X and Y values, respectively, of the N points used in the plot in question. The ranks are assigned such that $X(x_i) \leqslant X(x_{i+1})$ and $Y(y_i) \leqslant Y(y_{i+1})$, with "ties" assigned the average rank of the tied values. (Note that the rank order does not depend on whether we use the X_i values or their logarithms $\log_{10} X_i$.) The Spearman's rank correlation coefficient is then calculated as the correlation coefficient of the ranks:

$$\rho = \frac{\sum_{i=1}^{N} (x_i - \overline{x})(y_i - \overline{y})}{\sqrt{\sum_{i=1}^{N} (x_i - \overline{x})^2 \sum_{i=1}^{N} (y_i - \overline{y})^2}}, \tag{A6}$$

where $\overline{x}$ and $\overline{y}$ are the means of the ranks x_i and y_i, respectively. For a monotonic dependence of Y on X, $\rho = 1$, even if the variables do not obey a perfect linear correlation.

REFERENCES

Band, D., Matteson, J., Ford, L., et al. 1993, ApJ, 413, 281
Bobra, M. G., van Ballegooijen, A. A., & DeLuca, E. E. 2008, ApJ, 672, 1209
Brown, J. C. 1973, Sol. Phys., 28, 151
Brueckner, G. E., Howard, R. A., Koomen, M. J., et al. 1995, Sol. Phys., 162, 357
Caspi, A. 2010, PhD thesis, Univ. California
Caspi, A., & Lin, R. P. 2010, ApJ, 725, L161
Chamberlin, P. C., Milligan, R. O., & Woods, T. N. 2012, Sol. Phys., 279, 23
Chamberlin, P. C., Woods, T. N., & Eparvier, F. G. 2007, Space Weather, 50, 7005
Chamberlin, P. C., Woods, T. N., & Eparvier, F. G. 2008, Space Weather, 60, 5001
Chollet, E. E., Giacalone, J., & Mewaldt, R. A. 2010, J. Geophys. Res. (Space Phys.), 115, 6101
Cohen, C. M. S., Stone, E. C., Mewaldt, R. A., et al. 2005, J. Geophys. Res.(Space Phys.), 110, 9
Cook, W. R., Cummings, A. C., Cummings, J. R., et al. 1993, IEEE Trans. Geosci. Remote Sens., 31, 557
Culhane, J. L., Harra, L. K., James, A. M., et al. 2007, Sol. Phys., 243, 19
de Jager, C., Bruner, M. E., Crannell, C. J., et al. 1986, in Energetic Phenomena on the Sun, NASA Conf. Pub. 2439, ed. M. R. Kundu & B. E. Woodgate (Greenbelt, MD: NASA), 5.5
Dennis, B. R., & Pernak, R. L. 2009, ApJ, 698, 2131
Dere, K. P., Landi, E., Mason, H. E., Monsignori Fossi, B. C., & Young, P. R. 1997, A&AS, 125, 149
Dere, K. P., Landi, E., Young, P. R., et al. 2009, A&A, 498, 915
Doschek, G. A., Mariska, J. T., Watanabe, T., et al. 1992, PASJ, 44, L95
Ellison, D. C., & Ramaty, R. 1985, ApJ, 298, 400
Emslie, A. G., Dennis, B. R., Holman, G. D., & Hudson, H. S. 2005, J. Geophys. Res.(Space Phys.), 110, 11103
Emslie, A. G., Kucharek, H., Dennis, B. R., et al. 2004, J. Geophys. Res. (Space Phys.), 109, A10104
Feldman, U., Doschek, G. A., Behring, W. E., & Phillips, K. J. H. 1996, ApJ, 460, 1034
Garcia, H. A. 2004, Space Weather, 2, 2002
Gold, R. E., Krimigis, S. M., Hawkins, S. E., III, et al. 1998, Space Sci. Rev., 86, 541
Gopalswamy, N. 2006, J. Astrophys. Astron., 27, 243
Gopalswamy, N., Yashiro, S., Krucker, S., Stenborg, G., & Howard, R. A. 2004, J. Geophys. Res. (Space Phys.), 109, 12105
Gosling, J. T. 1993, J. Geophys. Res., 98, 18937
Grechnev, V. V., Kurt, V. G., Chertok, I. M., et al. 2008, Sol. Phys., 252, 149
Guo, J., Emslie, A. G., Massone, A. M., & Piana, M. 2012, ApJ, 755, 32
Guo, Y., Ding, M. D., Wiegelmann, T., & Li, H. 2008, ApJ, 679, 1629
Hua, X.-M., & Lingenfelter, R. E. 1987, Sol. Phys., 107, 351
Jiao, L., McClymont, A. N., & Mikic, Z. 1997, Sol. Phys., 174, 311
Kahler, S. W. 1982, J. Geophys. Res., 87, 3439
Kiener, J., Gros, M., Tatischeff, V., & Weidenspointner, G. 2006, A&A, 445, 725
Kontar, E. P., Brown, J. C., Emslie, A. G., et al. 2003, ApJ, 595, L123
Kontar, E. P., Brown, J. C., & McArthur, G. K. 2002, Sol. Phys., 210, 419
Kopp, G., & Lawrence, G. 2005, Sol. Phys., 230, 91
Lario, D., Kallenrode, M.-B., Decker, R. B., et al. 2006, ApJ, 653, 1531
Lemen, J. R., Duncan, D. W., Edwards, C. G., et al. 2004, Proc. SPIE, 5171, 65
Lemen, J. R., Title, A. M., Akin, D. J., et al. 2012, Sol. Phys., 275, 17
Li, G., Shalchi, A., Ao, X., Zank, G., & Verkhoglyadova, O. P. 2012, Adv. Space Res., 49, 1067
Lin, R. P. 2005a, in AIP Conf. Proc. 781, The Physics of Collisionless Shocks: 4th Annual IGPP International Astrophysics Conference, ed. G. Li, G. P. Zank, & C. T. Russell (Melville, NY: AIP), 246
Lin, R. P. 2005b, Adv. Space Res., 35, 1857
Lin, R. P., Dennis, B. R., Hurford, G. J., et al. 2002, Sol. Phys., 210, 3
Lin, R. P., Schwartz, R. A., Pelling, R. M., & Hurley, K. C. 1981, ApJ, 251, L109
Mason, G. M., Gold, R. E., Krimigis, S. M., et al. 1998, Space Sci. Rev., 86, 409
Mazzotta, P., Mazzitelli, G., Colafranceso, S., & Vittorio, N. 1998, A&AS, 133, 403

Metcalf, T. R., De Rosa, M. L., Schrijver, C. J., et al. 2008, Sol. Phys., 247, 269
Metcalf, T. R., Jiao, L., McClymont, A. N., Canfield, R. C., & Uitenbroek, H. 1995, ApJ, 439, 474
Metcalf, T. R., Leka, K. D., & Mickey, D. L. 2005, ApJ, 623, L53
Mewaldt, R. A. 2006, Space Sci. Rev., 124, 303
Mewaldt, R. A., Cohen, C. M. S., Cook, W. R., et al. 2008a, Space Sci. Rev., 136, 285
Mewaldt, R. A., Cohen, C. M. S., Giacalone, J., et al. 2008b, in AIP Conf. Proc. 1039, Particle Acceleration and Transport in the Heliosphere and Beyond, ed. G. Li, Q. Hu, O. Verkhoglyadova, G. P. Zank, R. P. Lin, & J. Luhmann (Melville, NY: AIP), 111
Mewaldt, R. A., Cohen, C. M. S., Labrador, A. W., et al. 2005, J. Geophys. Res. (Space Phys.), 110, 9
Mewaldt, R. A., Looper, M. D., Cohen, C. M. S., et al. 2012, Space Sci. Rev., 171, 97
Milligan, R. O., & Dennis, B. R. 2009, ApJ, 699, 968
Mishev, A. L., Velinov, P. I. Y., Mateev, L., & Tassev, Y. 2011, Adv. Space Res., 48, 1232
Moore, R., McKenzie, D. L., Svestka, Z., et al. 1980, in Skylab Solar Workshop II, ed. P. A. Sturrock (Boulder, CO: Colorado Associated Univ. Press), 341
Moore, R. L., Falconer, D. A., & Sterling, A. C. 2012, ApJ, 750, 24
Moraal, H., & McCracken, K. G. 2012, Space Sci. Rev., 171, 85
Morgan, T., & Lopate, C. 2008, in Proc. 30th Int. Cosmic Ray Conf., ed. R. Caballero et al., Vol. 1, 285
Müller-Mellin, R., Kunow, H., Fleißner, V., et al. 1995, Sol. Phys., 162, 483
Murphy, N. A., Raymond, J. C., & Korreck, K. E. 2011, ApJ, 735, 17
Murphy, R. J., Kozlovsky, B., Share, G. H., Hua, X.-M., & Lingenfelter, R. E. 2007, ApJS, 168, 167
Onsager, T., Grubb, R., Kunches, J., et al. 1996, Proc. SPIE, 2812, 281
Phillips, K. J. H., Feldman, U., & Landi, E. 2008, Ultraviolet and X-ray Spectroscopy of the Solar Atmosphere (Cambridge: Cambridge Univ. Press), 270
Pizzo, V. J., Hill, S. M., Balch, C. C., et al. 2005, Sol. Phys., 226, 283
Poland, A. I., Howard, R. A., Koomen, M. J., Michels, D. J., & Sheeley, N. R., Jr. 1981, Sol. Phys., 69, 169
Ramaty, R., & Mandzhavidze, N. 2000, in IAU Symp. 195, Highly Energetic Physical Processes and Mechanisms for Emission from Astrophysical Plasmas, ed. P. C. H. Martens, S. Tsuruta, & M. A. Weber (Cambridge: Cambridge Univ. Press), 123
Ramaty, R., Mandzhavidze, N., & Kozlovsky, B. 1996, in AIP Conf. Proc. 374, High Energy Solar Physics, ed. R. Ramaty, N. Mandzhavidze, & X.-M. Hua (Melville, NY: AIP), 172
Ramaty, R., Mandzhavidze, N., Kozlovsky, B., & Murphy, R. J. 1995, ApJ, 455, L193
Reames, D. V. 2009, ApJ, 693, 812
Rottman, G. J., Woods, T. N., & Sparn, T. P. 1993, J. Geophys. Res., 981, 10667
Saint-Hilaire, P., & Benz, A. O. 2002, Sol. Phys., 210, 287
Scherrer, P. H., Bogart, R. S., Bush, R. I., et al. 1995, Sol. Phys., 162, 129
Scherrer, P. H., Schou, J., Bush, R. I., et al. 2012, Sol. Phys., 275, 207
Schrijver, C. J., De Rosa, M. L., Metcalf, T. R., et al. 2006, Sol. Phys., 235, 161
Schrijver, C. J., De Rosa, M. L., Metcalf, T., et al. 2008, ApJ, 675, 1637
Shih, A. Y., Lin, R. P., & Smith, D. M. 2009, ApJ, 698, L152
Shih, A. Y.-M. 2009, PhD thesis, Univ. California
Simnett, G. M. 2006, A&A, 445, 715
Simnett, G. M. 2007, A&A, 472, 309
Stone, E. C., Cohen, C. M. S., Cook, W. R., et al. 1998, Space Sci. Rev., 86, 357
Su, Y., Dennis, B. R., Holman, G. D., et al. 2012, ApJ, 746, L5
Su, Y., Holman, G. D., & Dennis, B. R. 2011, ApJ, 731, 106
Thalmann, J. K., & Wiegelmann, T. 2008, A&A, 484, 495
Thalmann, J. K., Wiegelmann, T., & Raouafi, N. 2008, A&A, 488, L71
von Rosenvinge, T. T., Reames, D. V., Baker, R., et al. 2008, Space Sci. Rev., 136, 391
Vourlidas, A., Howard, R. A., Esfandiari, E., et al. 2010, ApJ, 722, 1522
Vourlidas, A., Howard, R. A., Esfandiari, E., et al. 2011, ApJ, 730, 59
Vourlidas, A., Subramanian, P., Dere, K. P., & Howard, R. A. 2000, ApJ, 534, 456
Welsch, B. T., Li, Y., Schuck, P. W., & Fisher, G. H. 2009, ApJ, 705, 821
White, S. M., Thomas, R. J., & Schwartz, R. A. 2005, Sol. Phys., 227, 231
Woods, T. N., Eparvier, F. G., Bailey, S. M., et al. 2005, J. Geophys. Res. (Space Phys.), 110, 1312
Woods, T. N., Eparvier, F. G., Hock, R., et al. 2012, Sol. Phys., 275, 115
Woods, T. N., Hock, R., Eparvier, F., et al. 2011, ApJ, 739, 59
Woods, T. N., Kopp, G., & Chamberlin, P. C. 2006, J. Geophys. Res. (Space Phys.), 111, 10